Energy Conversion and Management 344 (2025) 120330

Contents lists available at ScienceDirect

Energy Conversion and Management

journal homepage: www.elsevier.com/locate/enconman

Numerical, analytical and experimental thermodynamic analysis of the design of an innovative ring array concentrator solar system with solar furnace containing phase change material

Ali Kemal Özcan [a,*], Cevdet Demirtaş [b,†], Betül Saraç [b]

[a] Karadeniz Technical University, Dr., Trabzon, Hasan Kalyoncu University, Faculty of Engineering, Department of Mechanical Engineering, Gaziantep, Turkey
[b] Karadeniz Technical University, Department of Naval Architecture and Marine Engineering, Prof., Trabzon, Turkey

ARTICLE INFO

Keywords:
Ring array concentrator
Finned solar furnace
Thermal storage with salt
Energy and exergy analysis
Analytical solar radiation
Melting solidification simulation

ABSTRACT

The rising demand for reliable and sustainable renewable energy has increased the need for efficient thermal energy storage. This study introduces a novel solar furnace integrated with a Ring Array Concentrator (RAC) system—rarely explored in literature—and investigates high-temperature thermal storage using Phase Change Materials (PCM) through experimental and theoretical methods. Two solar storage units were developed: Model-I with a flat receiver and Model-II with finned cylindrical receiver for enhanced heat transfer. The newly developed RAC system was tested experimentally in the Trabzon province of Turkiye. Instantaneous solar irradiation for the region was also determined analytically. During a 10-hour operating period, Model-I successfully melted 0.7 kg of solar salt and 3.8 kg of Hitec salt. In contrast, the enhanced Model-II system achieved full melting of 18 kg of Hitec salt within 7 h, reaching an average temperature of 455 K. Experimental and numerical results revealed that the RAC system achieved an optical efficiency of 58.8 %, with the receiver efficiency calculated at 64.3 %. The maximum thermal efficiency and exergy efficiency of the solar furnace are determined to be 39 % with a 3.4 % uncertainty and 20 % with a 1.3 % uncertainty, respectively. A strong agreement was observed between experimental measurements and theoretical predictions for both furnace models. This work offers a novel and integrated solar thermal system by combining advanced RAC optics with PCM-based thermal storage, making a significant contribution to sustainable energy technologies through improved heat storage performance, reduced CO_2 emissions, and adaptability to varying environmental conditions.

1. Introduction

Solar energy is one of the most significant renewable energy sources in today's energy production landscape. Concentrated solar power (CSP) technologies are generally categorized into two main groups based on their focusing methods: line-focus and point-focus systems. Mwesigye et al., investigated the potential of nanotechnology to enhance the thermal performance of medium-temperature parabolic trough collectors operating under line-focus conditions [1]. Similarly, Achahour et al. demonstrated experimentally that Linear Fresnel.

Reflector (LFR) systems can be efficient in medium-temperature applications, and that integrating thermal energy storage systems provides a clear advantage in overall system efficiency [2]. Umar et al., further analyzed the role of thermal energy storage in improving the sustainability and efficiency of solar power plants [3]. These studies collectively highlight the key parameters such as working fluid type, nanoparticle additives, system design, and thermal storage integration that significantly influence the performance of concentrated solar systems, offering a solid scientific foundation for advancing solar technologies. Among point-focus systems, RAC, which function similarly to parabolic dish concentrators, have shown great potential for achieving high-temperature thermal storage, making them a promising alternative for advanced solar thermal applications. Vasylyev et al., demonstrated that RAC systems can be used to develop a new generation of High-Concentration Photovoltaic (HCPV) modules, achieving concentration ratios exceeding 1,000 while maintaining a uniform flux distribution [4]. This finding highlights the potential of RAC systems as efficient concentrators for high-performance photovoltaic applications. Similarly, Garcia et al., conducted an analytical study on a RAC system with a

* Corresponding author at: Karadeniz Technical University, Trabzon, Turkey.
E-mail addresses: ozcants61@gmail.com, akemal.ozcan@hsk.edu.tr (A.K. Özcan), bsarac@ktu.edu.tr (B. Saraç).
† This article is based on Ali Kemal Özcan's doctoral thesis. The advisor of this thesis was Assoc. Prof. Cevdet Demirtaş, who passed away in September 2024.

https://doi.org/10.1016/j.enconman.2025.120330
Received 16 April 2025; Received in revised form 3 August 2025; Accepted 3 August 2025
Available online 16 August 2025

Nomenclature

Latin characters

A_{sf}	Partial solid–fluid domain constant
$C_{p,PCM(s)}$	Constant pressure specific heat of PCM in solid state (J $kg^{-1}K^{-1}$)
$C_{p,PCM(l)}$	Constant pressure specific heat of PCM in liquid state (J $kg^{-1}K^{-1}$)
$E_{x,dest}$	Total exergy destruction per unit time (W)
$E_{x,in}$	Exergy entering the furnace per unit time (W)
$E_{x,out}$	Exergy from the furnace per unit time (W)
$E_{x,st}$	Exergy stored in the furnace per unit time (W)
$E_{x,loss}$	Total exergy loss per unit time (W)
F_1	Inertia resistance
fs x Γ	Shading and contrast factor
H	Molten material enthalpy (J kg^{-1})
h	Heat transfer coefficient from the focal area ($Wm^{-2}K^{-1}$)
h_s	Hour angle (°)
h_{ss}	Sunset hour angle (°)
I	Solar radiation (W m^{-2})
I_B	Direct radiation incident on inclined surface (W m^{-2})
I_g	Global radiation amount (W m^{-2})
I_D	Diffuse radiation incident on inclined surface (W m^{-2})
I_R	Reflected radiation from inclined surface (W m^{-2})
I_t	Total irradiance (W m^{-2})
K	Permeability resistivity in numerical calculation
k_f	Thermal conductivity coefficient of PCM in liquid state (W $m^{-1}K^{-1}$)
L_{sf}	Latent heat of melting (J kg^{-1})
l	Wall thickness for inorganic salt (m)
m	Inorganic salt mass (kg)
$\dot{m}$	Melting mass flow rate (kg s^{-1})
p	Internal pressure of the fluid (N m^{-2})
S	Source term
$\dot{s}_{gen}$	Entropy generation rate (W/K)
$\dot{Q}_{st}$	Energy stored in the system per unit time (W)
$\dot{Q}_{solar}$	Solar energy per unit time (W)
$\dot{Q}_L$	Energy lost from the furnace (W)
$\dot{Q}_{conv}$	Heat transfer by convection (W)
$\dot{Q}_{RAC}$	Heat transfer between system and surroundings (J)
t	Time (s)
T_1	Liquid temperature of inorganic salt (K)
T_i	Initial temperature of PCM (K)
T_a	Ambient temperature (K)
T_{foc}	Theoretical focal temperature (K)
V	Volume of inorganic salt (m^3)

Greek characters

α_s	Sun elevation angle (°)
α	Thermal diffusion coefficient (m^2 s^{-1})
α_r	Absorption rate of receiver surface
β	Inclination angle of receiver surface
β	Molten liquid fraction of an inorganic salt
β_{te}	Coefficient of thermal expansion (K^{-1})
ε_r	Emissivity coefficient
ε	Porosity coefficient
$\dot{\epsilon}$	A number too small to avoid division by zero
λ	Target angle (°)
μ_f	Dynamic viscosity of fluid (kg $m^{-1}s^{-1}$)
ρ_f	Density of inorganic salt in liquid state (kgm^{-3})
τ	Permeability coefficient
σ	Stefan − Boltzmann constant (W m^{-2} K^{-4})
$\vec{v_p}$	Solid speed in solidification (m s^{-1})
u	velocity component in the x-direction
v	velocity component in the y-direction
ν	Kinematic viscosity (m^2 s^{-1})
w	velocity component in the z-direction
∇	Gradient operator

concentrator surface area of approximately 3.14 m^2, reporting an exceptionally high theoretical concentration ratio of 30,960 [5]. Their study evaluated the applicability of this system using a small spherical receiver with a radius of just 5.68 mm. However, the extremely small receiver size limits the practical scalability and broader application of such systems. These studies collectively emphasize the promising concentration capability of RAC technologies, while also underlining the need for new design approaches to enhance their feasibility in large-scale thermal and photovoltaic applications. Garcia et al., evaluated the optical performance of concentrator systems composed of seven concentric parabolic reflector rings combined with a small Fresnel lens positioned at the center, utilizing Zemax ray-tracing software. Their numerical analyses revealed that most models achieved a concentrated solar flux exceeding 18 W mm^{-2} with an optical efficiency around 54 % [6]. This study underscores the potential of RAC systems to enhance optical efficiency through advanced high-concentration designs. In contrast, an experimental investigation by Ky et al., tested five RAC units, each with an aperture area of 1.692 m^2, under approximately 5.5 kWh m^{-2} day^{-1} solar irradiation in Burkina Faso. The systems, operating at an average geometric concentration ratio of 38, achieved a receiver temperature of 603 K and demonstrated a thermal efficiency of 40 %, confirming their suitability for cooking applications [7]. However, this work did not address thermal energy storage experimentally. In combination, these studies illustrate the versatility of RAC systems across high-efficiency optical concentration and practical thermal applications, while simultaneously highlighting a significant gap in the literature regarding the integration of thermal energy storage within such systems.

Solid–liquid PCMs used in thermal energy storage applications are generally classified into three categories: organic, inorganic, and eutectic mixtures Cabeza et al., provided a comprehensive review of the technical challenges encountered when implementing PCMs in building applications and proposed potential solutions to address these issues [8]. Jiang et al., demonstrated that a eutectic mixture of 43 % Potassium Carbonate (K_2CO_3), 57 % Sodium Carbonate (Na_2CO_3) and combined with Magnesium Oxide (MgO), maintained shape stability with up to 60 % PCM content, exhibiting a melting point of 983 K, an energy density of 431.2 J g^{-1}, and thermal stability up to 1158 K [9]. Furthermore, Tao et al., showed that magnetically actuated receivers suspended within molten salts heated by solar radiation can significantly enhance thermal energy storage rates [10]. These studies highlight the critical importance of selecting PCMs with high specific heat capacity, cost-effectiveness, and thermal stability for efficient thermal energy storage in solar energy systems, emphasizing that material choice directly influences overall system performance.

The geometry of the receiver plays a crucial role in maximizing the thermal efficiency of parabolic dish and RAC. Various receiver designs have been investigated in the literature, with Bellos et al., reporting that a cylindrical-conical receiver geometry achieved optimal performance, yielding thermal, exergy, and optical efficiencies of 67.9 %, 35.7 %, and 85.4 % respectively at 573 K [11]. Similarly, Kasaeian et al., demonstrated that a conical cavity receiver provided thermal and optical efficiencies of 70 % and 87 % respectively at an operating temperature of 473 K [12]. These studies collectively emphasize the importance of

carefully selecting receiver geometry according to the specific concentrator system, highlighting that cylindrical or spherical receivers may be more suitable for certain configurations.

Various thermal energy storage methods have been developed for solar-powered systems. Verma and Das demonstrated that a packed-bed thermal storage tank could support a solar desalination unit to produce 11.69 kg of potable water per cubic meter of storage volume [13]. In a related study, Verma et al., analytically investigated the cooking efficiency of a box-type solar cooker, revealing that the size of the cooking vessel significantly impacts both daytime and nighttime cooking performance [14]. Meanwhile, Asgari et al., showed that incorporating branched fins combined with 0.04 % hybrid Aluminum Oxide-Copper (Al_2O_3-Cu) nanoparticles into inorganic PCMs notably accelerated the solidification process and enhanced heat transfer rates [15]. Overall these studies highlight the critical role of thermal energy storage and fin design in improving the overall efficiency of PCM-based solar thermal systems.

In the selection of materials for furnace and fin components operating with molten salts, corrosion resistance is a critical factor. Ma et al., reported that stainless steel alloys 304 and 316L exhibit good mechanical properties and corrosion resistance up to 773 K [16]. Kruizenga et al., conducted 3,000-hour corrosion tests in a solar salt environment composed of 60 % by weight Sodium Nitrate ($NaNO_3$) and 40 % by weight Potassium Nitrate (KNO_3) on alloys including 347SS, 321SS, In625, and HA230. They observed the formation of thin oxide layers at 673 K, while at 773 K, iron-based alloys experienced chromium depletion and iron oxide formation [17]. Importantly, negligible metal dissolution was detected in the salt at these temperatures. Similarly, Zhu et al., demonstrated that 316SS maintains corrosion resistance in Hitec salt at 723 K [18]. Collectively, these findings support the preference for stainless steels in furnace construction for long-term, high-temperature applications.

In this study, an innovative solar furnace design featuring a RAC system—an area scarcely explored in the literature—was developed, and its thermal performance was comprehensively investigated through analytical, numerical, and experimental methods. The RAC arrangement, consisting of eight concentrator rings, focuses solar radiation beneath the rings to a specific focal region on the furnace, creating an effective localized heat source. Capitalizing on its high concentration ratio, superior optical properties, precise ray-tracing capability, and modular-compact structure, two PCM-compatible receiver designs were proposed: cylindrical solar furnace with flat receiver (Model-I) and cylindrical solar furnace with finned cylindrical receiver (Model-II). For energy storage, economically viable inorganic eutectic salts with high specific heat capacities, namely Hitec and solar salt, were selected. This holistic approach addressed not only heat collection but also the efficiency of thermal energy storage. Prior works by Vasylyev et al. [4] and Garcia et al. [5] highlighted RAC systems with exceptionally high concentration ratios but limited practical applications; additionally, by Ky et al. [7] experimentally demonstrated RAC use for cooking without exploring thermal storage integration, revealing a significant gap in the current literature. Moreover, the finned structure employed in Model-II draws on findings by Asgari et al. [15], who demonstrated enhanced heat transfer and efficiency in PCM-based systems using similar fin configurations. The selection of 304 and 316L stainless steel, known for its corrosion resistance and durability at elevated temperatures Ma et al. [16] further strengthens the system's longevity and reliability when operating with molten salts. Overall, this pioneering RAC-based solar furnace system represents the first of its kind in the literature to integrate optical and thermal analyses with inorganic PCM-based energy storage, offering a significant contribution towards sustainable energy generation, CO_2 emission reduction, and adaptability to diverse climatic conditions.

2. Material and method

In this section, the design and thermal performance analysis of two solar furnace configurations Model-I with a flat receiver and Model-II with an externally finned cylindrical receiver integrated with different phase change materials (solar salt and Hitec salt) are presented. Analytical and numerical evaluations of the thermal behavior of both systems are conducted in detail. Additionally, the experimental setup developed for the novel RAC-integrated solar furnace system is introduced, providing a comprehensive overview of the methodology used to assess the system's performance.

2.1. Materials

The newly developed RAC-solar furnace system features an innovative ring array concentrator design composed of eight concentric reflective rings and a solar furnace located at the focal area, which incorporates PCMs for efficient thermal energy storage.

2.1.1. Introduction of ring array concentrator

The newly designed and manufactured solar concentrator system, featuring the RAC composed of eight geometrically distinct rings, focuses sunlight onto a central receiver by concentrating solar rays along the inner surface of each ring. This configuration enables the attainment of high temperatures at the receiver surface. The surface curvatures of the concentrator rings and the spacing between them were precisely designed using Solidworks software. A schematic illustration of the system is presented in Fig. 1. During the fabrication process, cross-sectional profiles of approximately 250 mm in size were created using a 3D printer and used as molds for the sloped surfaces. The parabolic truncated conical rings were formed by pouring epoxy resin over fiberglass within these molds. After curing, the components were carefully assembled to produce lightweight and easily mountable concentrator rings. However, in order to ensure accurate focusing of the solar rays at the designated focal point, the assembly of the rings must be carried out with high precision using laser alignment.

By adjusting the diameter of the focal zone, the focal temperature of the system can be effectively controlled. As the focal length increases, the inclination angles of the ring concentrators relative to the horizontal axis also increase, allowing more rings to be positioned per unit area and thereby enhancing the total radiation-receiving surface. Consequently, by reducing the edge angle (θr) and improving the optical efficiency, both the temperature and thermal energy at the focal region can be significantly increased. The geometric design parameters of the RAC model such as top and bottom diameters, curvature radii, reflective surface areas, and edge angles are detailed in Table 1.

To determine the optimal aperture area on the receiver surface, theoretical calculations were conducted to evaluate the focal temperatures corresponding to different concentration ratios. Fig. 2 presents a comparative graph of these results. Based on the analysis, the system identified as Type 2, with a concentration ratio of approximately 80, yielded a focal temperature of 570 K by Eq. (3). Considering the decomposition temperatures of the inorganic salts used (up to 873 K) and the thermal conductivity properties of the materials employed at the focal point, the optimal focal aperture diameter was determined to be in the range of 100–120 mm. The graph clearly shows that as the concentration ratio increases, the focal temperature rises, but the focal area becomes narrower highlighting a critical design trade-off. Additionally, the general features of the designed RAC system are given in Table 2.

On July 15, under the climatic conditions of a temperate region, the solar altitude angle varied within approximately $\pm 10^{\circ}$ between 10:30 and 15:30. hence, numerical analyses assumed a vertically oriented system under direct normal irradiance conditions. In the RAC design, solar rays reflected from the inner surfaces of the parabolic ring concentrators were effectively concentrated beneath each ring and directed toward the focal zone, where they were absorbed by the receiver

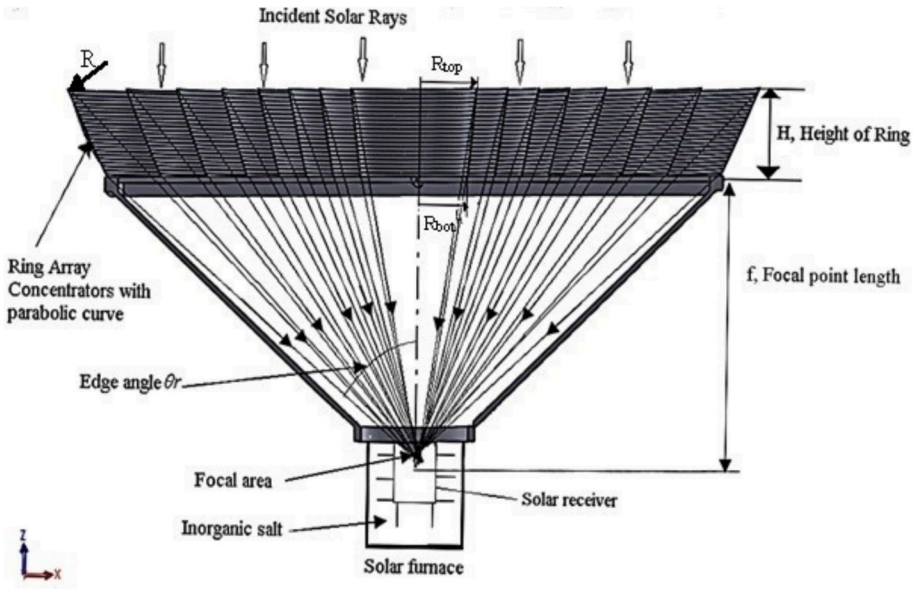

Fig. 1. The schematic showing the focusing of rays into the designed furnace by the RAC.

Table 1
Design features of the new Ring Array Concentrator model.

Number of rings	Radius of curvature (m)	Ring bottom diameter (m)	Ring top diameter (m)	RAC surface area (m^2)	Rim angle (°)
Ring 1	17.081	0.4	0.4683	0.0466	14.04
Ring 2	12.04	0.6	0.7008	0.1034	20.56
Ring 3	9.743	0.8	0.9314	0.179	26.57
Ring 4	8.5205	1	1.1602	0.271	32.01
Ring 5	7.521	1.04	1.4313	0.401	37.78
Ring 6	7.1783	1.34	1.7664	0.587	43.91
Ring 7	6.962	1.68	2.1401	0.822	49.54
Ring 8	6.965	2.2821	2.5761	1.12	54.94

typically a metallic or quartz-glass material positioned at the upper surface of the furnace. Compared to conventional parabolic dish concentrators, the RAC system offers several distinct advantages: larger receiver sizes can be used, enabling extended thermal storage durations; the need for frequent positional adjustment of the furnace is minimized; and proximity to the ground provides more ergonomic handling of thermal processing tasks. The assembled system and its solar tracking mechanism are illustrated in Fig. 3.

The tracking mechanism, which operates along the east–west axis with an angular range of approximately 120°, includes two 20 W actuators, a light-sensing sensor, and a control unit equipped with a wind-speed monitor. The system can be powered by a 12 V DC battery and operated either manually via remote control or automatically. Fig. 4 displays the photograph of the eight-ring concentrator array used in the experimental setup.

Table 2
Properties of the designed RAC systems.

Properties	RAC
Number of rings	8 Rings
Focal point length, f (cm)	80 ±1
Ring height, H (cm)	30 ±0.5
Total concentrator area, A_{RAC} (m^2)	3.5 ±0.02
Concentration ratio, C_R	(80 ±10)
Rim angle for end ring, θr (°)	54.94 ±0.5
Heat flux at the focal, q^1 (W/cm^2)	1.205 ±0.005

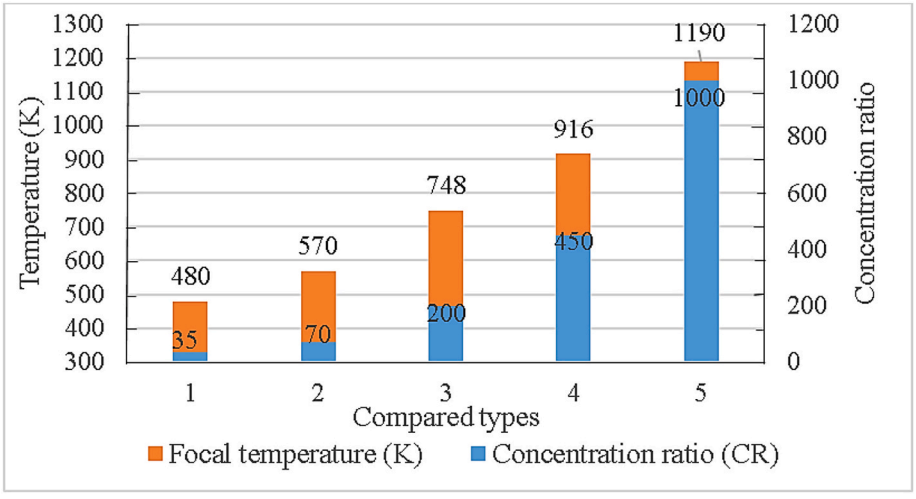

Fig. 2. Focus temperatures calculated according to different concentration ratios.

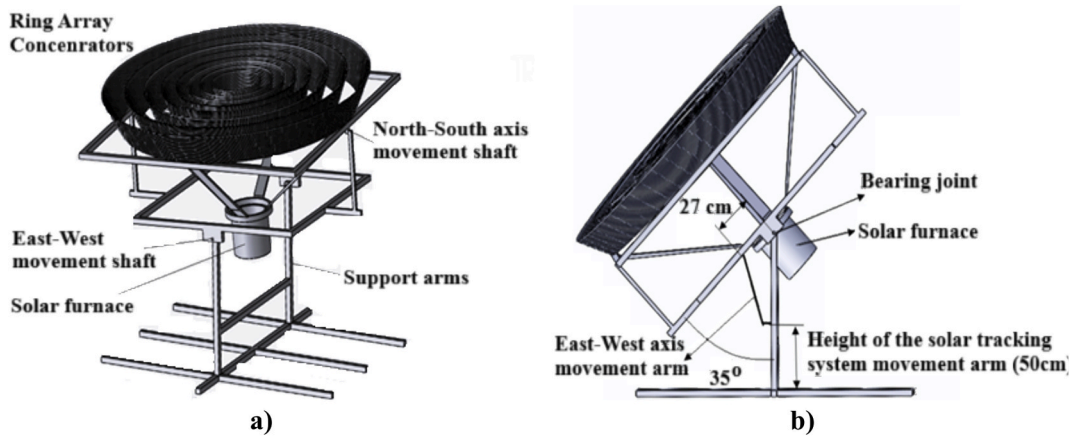

Fig. 3. Designed RAC-furnace system; a) General view of the manufacturing and assembly b) Side view of the system for the application of the sun tracking mechanism.

Fig. 4. Photo of eight-ring RAC system.

2.1.2. Solar furnace units

Inorganic salts used as PCMs are melted by conduction through concentrated solar rays directed by the RAC system. The aim is to achieve complete melting of the salt within a single day. Both solar furnaces are constructed from corrosion-resistant AISI 304 stainless steel, with dimensions of 260 mm diameter, 200 mm height, and 2 mm wall thickness. Model-I (12 L volume) features a flat 0.2 mm thick stainless steel receiver with a 100 mm focal surface diameter and is shown in Fig. 5a. Model-II (9 L volume) incorporates a hollow cylindrical receiver (100 mm diameter, 120 mm length, 0.2 mm thickness) placed inside the furnace and is shown in Fig. 5b. To enhance heat transfer, Model-II includes 24 fins (20 mm wide, 50 mm long) spaced 40 mm apart, doubling the effective surface area to 0.0507 m^2 and accelerating the salt melting rate. The furnace is insulated on the sides and bottom, with heat loss assumed only through the top focal surface.

2.1.3. Phase change materials

In this study, two different (PCMs) were employed. The first PCM, an inorganic eutectic mixture known as Solar Salt, consists of 50 % by weight Sodium Nitrate ($NaNO_3$) and 50 % by weight Potassium Nitrate (KNO_3), with a melting point of 222 °C. Its detailed thermophysical properties are listed in Table 3. The second PCM, Hitec Salt, is composed of 53 % by weight Potassium Nitrate (KNO_3), 40 % by weight Sodium Nitrite ($NaNO_2$), and 7 % by weight Sodium Nitrate ($NaNO_3$). The thermophysical properties of Hitec Salt are provided in Table 4.

2.2. Methods

In this section, the thermal performance of the newly developed RAC-Solar furnace system is comprehensively evaluated through analytical modeling, numerical simulations, and experimental validation.

2.2.1. Analytical calculation and available correlation

The geometric parameters of the RAC, focal region temperature, and instantaneous solar irradiance were determined based on established correlations from the literature. Additionally, this section presents the analytical temperature distribution of the inorganic salts within the solar furnaces, along with a comprehensive thermodynamic analysis of the overall system.

2.2.1.1. Geometric Dimensioning of Ring Array concentrator. The control volume for the RAC system is shown in Fig. 6. The total concentration ratio C_R used for the geometric and performance analysis of the ring arrays was calculated using Eq. (1) [22].

$$C_R = \frac{\sum_1^n A_{RAC,i}}{A_r} \tag{1}$$

where, Ar is the focal surface area on the receiver furnace, A_{RAC} is the total aperture surface area of concentrators and is determined by Eq. (2).

$$A_{RAC} = \pi \times \left[\left(R_{n,top}^2 - R_{n,bottom}^2 \right) + .. + \left(R_{1,top}^2 - R_{1,bottom}^2 \right) \right] \tag{2}$$

where, R_{top} and R_{bottom} denote the radial distances from the top and bottom edges of each ring to the focal axis, respectively. The theoretical average focal temperature T_{foc} was calculated using Eq. (3) [23], which incorporates optical efficiency, solar irradiance, and material properties:

$$T_{foc} = \left(\sqrt[4]{\frac{\eta_{op} \times \alpha_r \times \tau \times I \times C_R}{\varepsilon_r \sigma}} \right) \times F_D \times R_C \tag{3}$$

Based on preliminary experiments, T_{foc} was approximately 550 K,

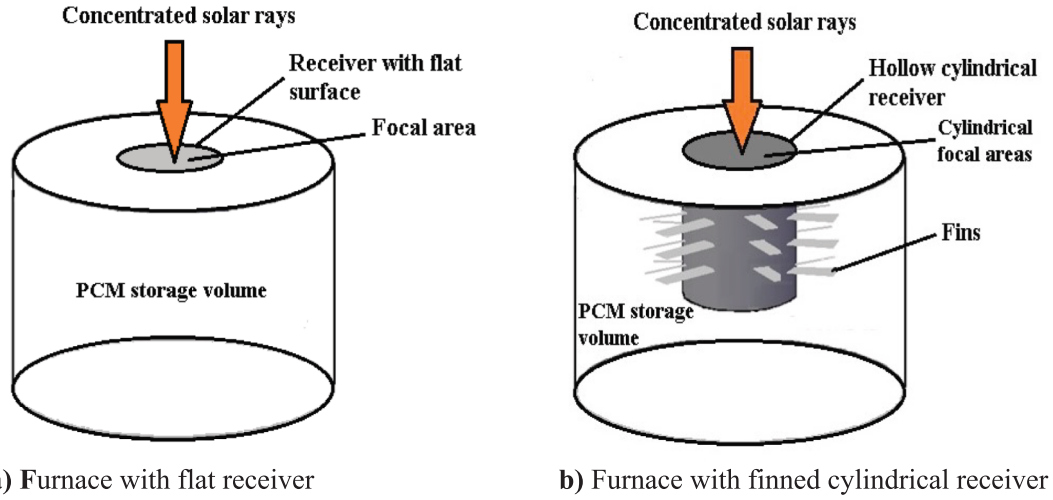

Fig. 5. A) image of model-i furnace with flat receiver, b) image of model-ii furnace with finned cylindrical receiver.

Table 3
Some physical characteristics of eutectic solar salt [19,20].

Parameters	Symbols	Values
Density (solid–liquid)	ρ	(2173.7–1836) kg m^{-3}
Specific heat (solid–liquid)	c_p	(1050–1500) J $kg^{-1}K^{-1}$
Thermal conductivity coefficient (solid–liquid)	k	(0.380–0.460) W m^{-1} K^{-1}
Latent heat	L_{sf}	110000 J kg^{-1}
Viscosity (liquid)	μ	(0.0033–0.00099) kg $m^{-1}s^{-1}$
Maximum operating temperature	T_b	838 (K)

corresponding to $F_D \times R_C \approx 0.55$. With minimal reflection and absorption losses, degradation factor F_D ranged between 0.85 and 0.9 and the cooling coefficient R_C between 0.6 and 0.7. Additional parameters used in in Eq. (3) are given in Table 5.

The thermal conversion efficiency of the RAC-solar receiver system is defined in Eq. (4), incorporating the optical, receiver, and Carnot efficiencies [5,24].

$$\eta_{solar,th} = \eta_{op} \times \eta_{rec} \times \eta_{Carnot} \tag{4}$$

The optical efficiency of RAC (η_{op}) depends on concentrator reflectivity ρ_{ch}, incidence angle θi, shading and contrast factors ($f_s\Gamma$), as expressed in Eq. (5) [23,25].

$$\eta_{op} = cos\theta i \times \rho_{ch} \times (f_s\Gamma) \tag{5}$$

The solar receiver efficiency of the current system depends on the optical efficiency, concentration ratio, absorption coefficient (α_r) of receiver, solar radiation, natural convection loss and radiation loss of focal surface. The solar receiver efficiency η_{rec} of the RAC system is calculated by Eq. (6).

Table 4
Some physical properties of Hitec salt [19,21].

Parameters	Symbols	Values
Density (solid–liquid)	ρ	(2013–1857) kg m^{-3}
Specific heat (solid–liquid)	c_p	(1090–1570) J $kg^{-1}K^{-1}$
Thermal conductivity coefficient (solid–liquid)	k	(0.74–0.439) W m^{-1} K^{-1}
Latent heat	L_{sf}	83740 J kg^{-1}
Viscosity (liquid)	μ	(0.024–0.0012) kg $m^{-1}s^{-1}$
Melting point temperature	T_m	415 (K)
Maximum operating temperature	T_b	811 (K)

$$\eta_{rec} = \alpha_r - \frac{Q_L}{\dot{E}_{in,RAC}} = \alpha_r - \frac{hA_r(T_{foc} - T_a) - A_r\,\varepsilon\,\sigma\left(T_{foc}^4 - T_a^4\right)}{IA_{RAC}} \tag{6}$$

where Q_L is the energy lost from the focal surface by convection and radiation and $\dot{E}_{in,RAC}$ is the total incident solar energy on the RAC systems.

Lastly, Carnot efficiency is defined by Eq. (7).

$$\eta_{Carnot} = 1 - \frac{T_a}{T_{foc}} \tag{7}$$

2.2.1.2. Analytical calculation of instantaneous solar radiation. The instantaneous average solar intensity value is equal to the sum of direct radiation, diffused radiation and reflected radiation values and are calculated by Eqs. (8), (9) and (10), respectively [29].

$$I_B = (r_t \times I_h - r_d \times I_d) \times \frac{cos\theta i}{\sin\alpha_s} \tag{8}$$

$$I_D = (r_d \times I_d) \times cos^2\left(\frac{\beta}{2}\right) \tag{9}$$

$$I_R = \rho_{gr} \times r_t \times I_h \times sin^2\left(\frac{\beta}{2}\right) \tag{10}$$

Additionally, r_d is the ratio of long-term hourly diffuse irradiance to daily average diffuse irradiance on a horizontal surface and is calculated by Eq. (11) [30,31,32]. Also r_t, which is the ratio of long-term hourly total radiation to the average daily total irradiation on a horizontal surface, was calculated with Eq. (12) [33,34].

$$r_d = \frac{\pi}{24} \times \frac{\cos(hs) - \cos(h_{ss})}{\sin(h_{ss}) - \frac{\pi}{180}(h_{ss}) \times \cos(h_{ss})} \tag{11}$$

$$r_t = (a + b \times \cos(hs)) \times r_d \tag{12}$$

where, the terms a and b in Eq. (12) are calculated with Eqs. (13) and (14), respectively [29].

$$a = 0.409 + 0.5016 \times \sin(hss - 60^\circ) \tag{13}$$

$$b = 0.6609 + 0.4767 \times \sin(hss - 60^\circ) \tag{14}$$

The hourly average diffuse radiation amount I_d incident on a horizontal surface is calculated with Eq. (15) depending on the global radiation amount and sky clarity index [35].

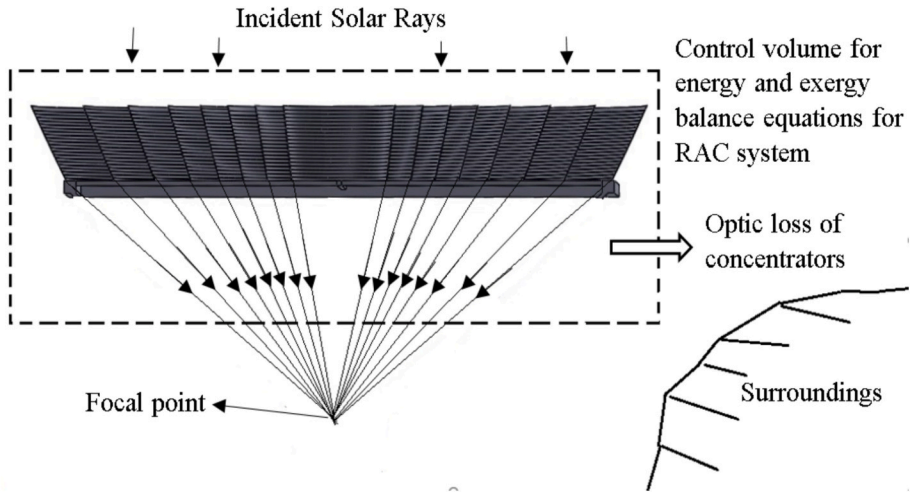

Fig. 6. View of the control volume selected for the RAC system.

Table 5
Parameters used in the design and their values.

Parameters	Symbols	Values
Reflectance coefficient	ρ_{ch}	0.95 ±0.03 (Nickel-Chromium-foil)
Beam shear angle	θi	0° ±5° (Perpendicular incident beam)
Absorption coefficient	α_r	0.89 ±0.05 (Solar salt) [26] 0.9 ±0.05 (Hitec salt) [27] 0.60 ±0.05 (steel) [28]
Emission coefficient	ε_r	0.89 ±0.05 (Solar salt) [26] (0.6–0.8) (Hitec salt) [27] (0.33–0.57) (steel) [28]

$$\frac{I_d}{I_g} = 0.785 - 0.803 \times k_T \tag{15}$$

For July noon in Trabzon, the k_T hourly sky clarity index was taken as 0.524 [35]. In addition, for July 15, at noon (hour angle at 12.30, hs = 0°), sunset hour angle (hss = 110°), sun elevation angle (αs = 70°), receiver surface inclination angle (β = 20°), for concrete ground with the reflection coefficient (ρ_{gr}= 0.22) values, the instantaneous average radiation amount coming to the inclined surface was calculated as 1006 W m^{-2}.

2.2.1.3. Calculation of temperature distribution and melting flow rate in solar furnaces. The heat conduction equation, a partial differential equation, describes the temporal evolution of temperature distribution within a non-homogeneous medium. In phase change processes involving melting or solidification, the governing heat transfer equation is formulated in terms of total volumetric enthalpy and temperature, as expressed in Eq. (16) below [36].

$$\frac{\partial H}{\partial t} = \nabla(k_k(\nabla T)) \tag{16}$$

In the term on the right side of the equation, conductivity (k) varies depending on the temperature gradient (∇T). This makes the material inhomogeneous. In order to solve the equation analytically, the equation was simplified by transforming it into a one-dimensional heat conduction equation depending on the initial and boundary conditions. In addition, assuming that the PCM was initially in solid state, it was calculated with Fourier's law, which is the wall heat conduction equation.

The control volume selected for the solar furnace is shown in Fig. 7. The energy coming to the focal surface on both types of furnaces (Model-I and Model-II) whose surroundings are insulated, is transferred to the PCM inside the furnace. The thermal energy stored on the PCM was equalized to the energy transferred by conduction, and the temperature distribution in the furnace was simplified and calculated with Eq. (17) [15].

$$\rho V c_p \frac{dT}{dt} + \rho V L_{sf} \frac{d\beta(T)}{dt} = \frac{-kA}{l}(T - T_{foc}) \tag{17}$$

Initially, it is assumed that PCM temperature is T = 300 K and focal temperature is T_{foc} = 500 K at t = 0, and specific heat (c_p) and thermal conductivity coefficient (k) of PCM changed depending on PCM temperature. β, which represents the liquid fraction of the phase change material, was defined by the following relation with Eq. (18) depending on the temperature [15].

$$\beta(T) = \frac{\left(T - T_m + \frac{T_0}{2}\right)}{T_0}; if \beta = 0, T < (T_m - T_0) and if \beta = 1, T > (T_m + T_0) \tag{18}$$

Thus, the equation in differential form was solved by writing the β term in terms of temperature (T). The melting point for Hitec salt is T_m = 415 K and the T_0 value is found to be 8 K because the melting is completed at 423 K. The value of the solid part of the inorganic salt is defined as S = (1-β). The value of the molten liquid portion of the inorganic salt is defined as the liquid phase for β = 1 and the solid phase for β = 0. The terms on the left are grouped to obtain the equation dT/dt. Thus, the relationship between temperature and time is obtained by integrating separately according to the variables of both sides. Finally, the analytical general solution in Eq. (19) is obtained to find the time-dependent furnace internal temperature distribution.

$$T = T_{foc} - e^{-\frac{kA\,t}{l\left(\rho V c_p + \frac{\rho V L_{sf}}{8}\right)} + C} \tag{19}$$

where C is the integral constant and was determined according to the initial conditions. By determining the initial conditions and the values of the constants, specific solutions are obtained for both Hitec salt and solar salt.

2.2.1.4. Thermodynamic analyses. Energy and exergy analyses for the RAC and solar furnace are given below.

2.2.1.4.1. Exergy and energy analyses of ring array concentrator. The solar energy coming to the RAC system was determined depending on the radiation surface area of the system. The output energy was calculated depending on the optical efficiency of the RAC system.

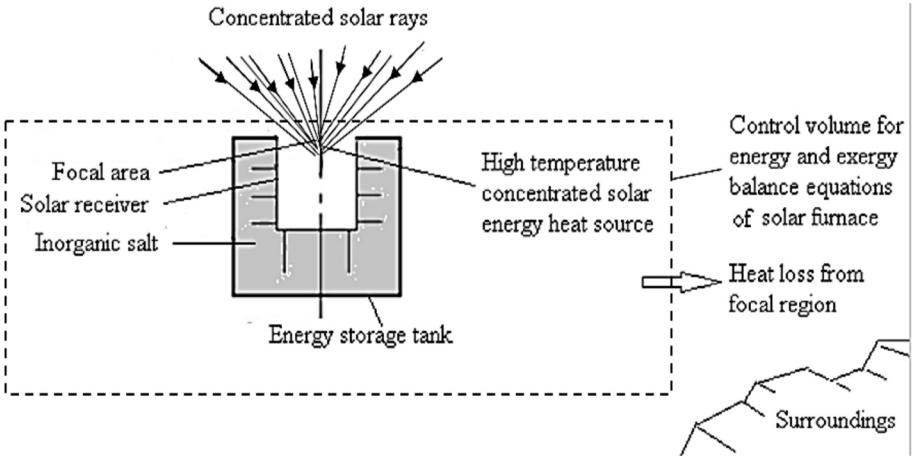

Fig. 7. View of the control volume selected for the solar furnace.

Accordingly, the First Law of Thermodynamics efficiency was calculated with the following Eq. (20) for the RAC system [37,38].

$$\eta_{RAC} = \eta_{op} = \frac{\dot{Q}_{out,RAC}}{\dot{Q}_{in,RAC}} = \frac{IA\eta_{op}}{IA} \tag{20}$$

The exergy efficiency of RAC systems is expressed by Eq. (21) as the ratio of the exergy leaving the concentrator (exergy coming to the focal point) to the exergy coming to the concentrator [39].

$$\psi_{RAC} = \frac{\dot{E}_{xout,RAC}}{\dot{E}_{xin,RAC}} = \frac{A_{RAC}I\eta_{op}\left[1-\frac{4T_a}{3T_{sol}}+\left(\frac{1T_a}{3T_{sol}}\right)^4\right]\left(1-\frac{T_a}{T_{foc,max}}\right)}{A_{RAC}I[1-\frac{4T_a}{3T_{sol}}+(\frac{1T_a}{3T_{sol}})^4]} \tag{21}$$

2.2.1.4.2. Energy analysis of solar furnace. The amount of energy stored in the inorganic salt as PCM was calculated based on the average temperature of the PCM. Thus, the total energy stored in the PCM during the solid–liquid phase change in the solar furnace is given by Eq. (22) [40–43]

$$Q_{st} = \int_{T_i}^{T_m} \dot{m}C_{pcm(s)}dT + \dot{m}L_{sf} + \int_{T_m}^{T_l} \dot{m}C_{pcm(l)}dT \tag{22}$$

The storage efficiency of the furnace is the ratio of useful energy to solar energy coming into the furnace. The instantaneous first law of Thermodynamics (η_{fur}) efficiency of the furnace was calculated with Eq. (23) [39].

$$\eta_{fur} = \frac{\dot{Q}_{st}}{\dot{Q}_{solar,fur}} = \frac{\dot{m}C_{pcm(s)}(T_m - T_i) + \dot{m}C_{pcm(l)}(T_l - T_m) + \dot{m}L_{sf}}{A_{RAC}I\eta_{op}\alpha_s} \tag{23}$$

where T_m is the melting point temperature of the salt and T_l is the highest liquid temperature of the salt. Analytically, maximum the solar intensity (I) is calculated as 1006 W m^{-2}.

2.2.1.4.3. Exergy analysis of the solar furnace. Heat is transferred to a certain volume of inorganic salt in the furnace, and the temperature of the salt increases with time. Thus, the entropy of the system increases as the temperature of the inorganic salt increases and the salt melts. The exergy efficiency of the RAC-solar furnace systems is defined by the increase in the exergy of the solar radiation source on the phase change material. Therefore, the exergy balance relation between total input exergy, total stored exergy, total exergy loss and total exergy destruction is given by Eq. (24) for closed systems.

$$\sum E_{x,in} = \sum E_{x,st} + \sum E_{x,loss} + \sum E_{x,dest} \tag{24}$$

where, $E_{x,dest}$ which represents the total exergy destruction (irreversibility) of the solar furnace is calculated by the following Eq. (25) [44].

$$\dot{E}_{x,dest} = T_a\dot{s}_{gen} \tag{25}$$

The entropy generation ($\dot{s}_{gen}$) of the closed RAC-furnace system is calculated by Eq. (26) [45].

$$\dot{s}_{gen} = (\Delta s_{system} + \frac{\dot{Q}_L}{T_a} - \frac{\dot{Q}_{RAC}}{T_{foc}}) \tag{26}$$

Considering that the RAC-furnace system has very little energy loss to the environment, it is assumed that there is no entropy change $\left(\frac{\dot{Q}_L}{T_a}\right)$ of the environment by taking it as adiabatic. However, there are radiation and natural convection losses from the focal surface above the furnace. In addition, since there is heat transfer from the RAC to the solar furnace system, the entropy change $(\frac{\dot{Q}_{RAC}}{T_{foc}})$ of the RAC system is added to the entropy generation connection. In a phase change of incompressible substances, the entropy change connection of the RAC-furnace system can be calculated by Eq. (27).

$$\Delta s_{system} = \dot{m}(s_2 - s_1) = \dot{m}(c_p \ln\frac{T_l}{T_i}) \tag{27}$$

The total exergy loss from the focal outer surface of the solar furnace was calculated by Eq. (28) [44].

$$\dot{E}_{x,loss} = \dot{Q}_L \times \left(1 - \frac{T_a}{T_{foc}}\right) \tag{28}$$

The heat loss by the emitted and reflected radiation from the focal surface on the solar furnace was calculated by Eq. (29) [38].

$$\dot{Q}_{Rad} = \dot{Q}_{R,e} + \dot{Q}_{R,ref} \tag{29}$$

The exergy stored of the phase change material in the RAC-Furnace system is given by Eq. (30) [44].

$$\dot{E}_{x,st} = \dot{m}_s C_{pcm(s)}(T_m - T_i) + \dot{m}_l C_{pcm(l)}(T_l - T_m) - \dot{m}_l T_a C_p \ln\left(\frac{T_l}{T_i}\right) + \dot{m}L_{sf}\left(1 - \frac{T_m}{T_l}\right) \tag{30}$$

The total net exergy entering the solar furnace was calculated by Eq. (31) [39,46].

$$\dot{E}_{x,in} = A_{RAC}I\eta_{op}\alpha_s[1 - \frac{4T_a}{3T_{sol}} + (\frac{1T_a}{3T_{sol}})^4](1 - \frac{T_a}{T_{foc,max}}) \tag{31}$$

where T_{sol} is the surface temperature of the Sun (6000 K), T_a is the ambient temperature (300 K). $T_{foc,max}$ is the maximum temperature (K)

achieved at the focal area.

Exergy efficiency was determined according to the useful heat of the PCM in the solar furnace, taking into account the solar energy input depending on the ambient temperature and surface temperature. If the input exergy is constant, the exergy efficiency of the designed solar furnace was calculated as the ratio of the stored exergy to the input exergy by Eq. (32) [39,46].

$$\psi_{Fur} = \frac{\dot{E}_{x,in} - \dot{E}_{x,loss}}{\dot{E}_{x,in}} = \frac{\dot{E}_{x,st}}{\dot{E}_{x,in}} \tag{32}$$

2.2.1.4.4. Energy and exergy analyses of total ring array Concentrator and solar furnace system. The total thermal energy efficiency of the RAC-solar furnace system is calculated as the ratio of the thermal energy stored in the furnace to energy coming to the RAC system with Eq. (33). The control volume selected for the RAC-solar furnace system is shown in Fig. 8.

$$\eta_{RAC,Fur} = \frac{\dot{Q}_{st}}{\dot{Q}_{in,RAC}} = \frac{\dot{m}C_{pcm(s)}(T_m - T_i) + \dot{m}C_{pcm(l)}(T_l - T_m) + \dot{m}L_{sf}}{IA} \tag{33}$$

The total exergy efficiency of the RAC-solar furnace system is calculated by Eq. (34).

$$\psi_{RAC,Fur} = \frac{\dot{E}_{x,st}}{\dot{E}_{xin,RAC}} = \frac{\dot{m}_s C_{pcm(s)}(T_m - T_i) + \dot{m}_l C_{pcm(l)}(T_l - T_m) - \dot{m}_l T_a C_p \ln\left(\frac{T_l}{T_i}\right) + \dot{m}L_{sf}\left(1 - \frac{T_m}{T_l}\right)}{A_{RAC} I \left[1 - \frac{4T_a}{3T_{sol}} + \left(\frac{1T_a}{3T_{sol}}\right)^4\right]} \tag{34}$$

2.2.2. Numerical method

The numerical modeling and simulation of the PCMs used in the solar furnace were performed using the melting and solidification model available in ANSYS Fluent. Among the various numerical techniques for PCM analysis, the Enthalpy–Porosity Method was employed in this study. This widely used approach models the melting/freezing process by incorporating latent heat effects and establishing a relationship between temperature and enthalpy to define the mushy region (the phase change zone where both solid and liquid coexist).

Other common numerical techniques in PCM modeling include:

- The Equivalent Heat Capacity (EHC) method, which simplifies the energy equation for small phase transition zones;
- The Volume of Fluid (VOF) method, suitable for simulating multi-phase (liquid–gas) flows;
- The Lattice Boltzmann Method (LBM), often used for microscale flows or complex geometries involving phase change;
- The Front Tracking Method (FTM), ideal for high-accuracy micro-scale solidification and melting processes; and
- The Level Set/Phase Field Methods, which are used for visualizing and tracking clear phase interfaces during microstructural transformations.

In this study, the following assumptions were made for the numerical simulations:

1. The standard melting and solidification assumptions of ANSYS Fluent were applied. Using melting enthalpy, the enthalpy values of solid and liquid phases were iteratively updated according to the computed liquid fraction (ranging from 0 to 1). In regions where solidification occurs, permeability is zero and fluid velocity drops accordingly [47,48,49].
2. Both 2D and 3D models were considered as transient processes.
3. The flow of molten salt (PCM) was assumed to be laminar, Newtonian, and incompressible.
4. The density and thermal conductivity of the PCM were modeled as linearly varying with temperature, while viscosity was considered temperature-dependent.

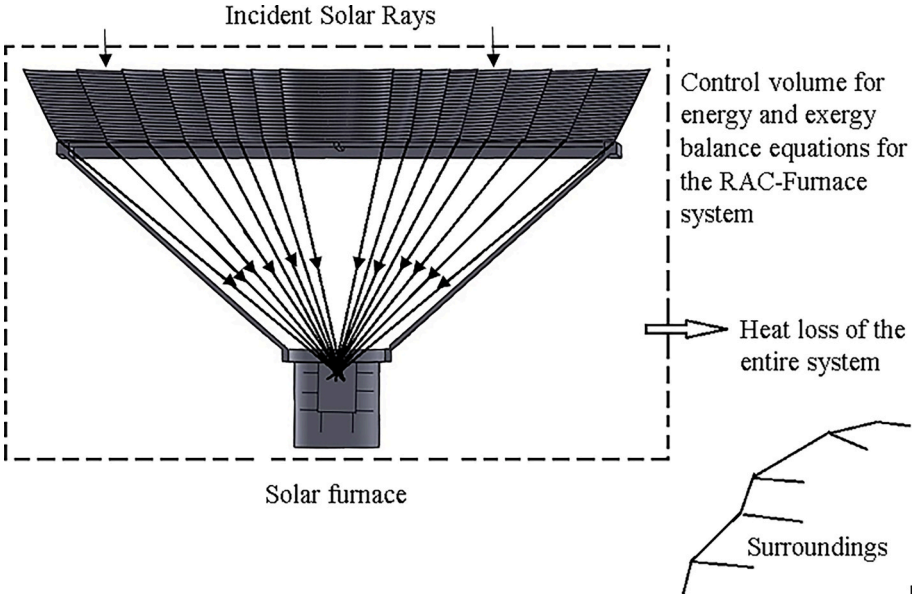

Fig. 8. View of the control volume selected for the RAC-Solar furnace system.

5. Heat transfer occurred via both conduction and natural convection. Since the volumetric expansion of the selected PCMs is negligible below 500 K, and the solar furnace operates under atmospheric pressure, this was also assumed in the model.
6. No internal heat generation was considered within the PCM domain of the furnace

2.2.2.1. Foundation equations. In modeling the solidification/melting time in ANSYS Fluent, the enthalpy-porosity technique is used, which realistically reflects the phase transition process [50]. For melting and solidification problems, the energy equation is solved by Eq. (35) [50], the continuity equation by Eq. (36) and the momentum equations by Eq. (37) in the x direction, Eq. (38) in the y direction and Eq. (39) in the z direction. is formulated [51].

Energy equation:

$$\frac{\partial(\rho_f H)}{\partial t}+\nabla.\left(\rho_f \vec{U}H\right)=\nabla.(k_f\nabla T)+S \tag{35}$$

Continuity equation:

$$\frac{\partial \rho_f}{\partial t}+\nabla\left(\rho_f \vec{U}\right)=0 \tag{36}$$

Momentum equations:

$$\frac{\rho}{\varepsilon}\frac{\partial u}{\partial t}+\frac{\rho_f}{\varepsilon^2}\left(\vec{U}\nabla u\right)=-\frac{\partial p}{\partial x}+\frac{\mu_f}{\varepsilon}\nabla^2 u-\left(\frac{\mu_f}{K}+\frac{\rho_f F_1}{\sqrt{K}}|u|\right)u+A_s u \tag{37}$$

$$\frac{\rho}{\varepsilon}\frac{\partial v}{\partial t}+\frac{\rho_f}{\varepsilon^2}\left(\vec{U}\nabla v\right)=-\frac{\partial p}{\partial y}+\frac{\mu_f}{\varepsilon}\nabla^2 v-\left(\frac{\mu_f}{K}+\frac{\rho_f F_1}{\sqrt{K}}|v|\right)v+\rho_f g\beta_{te}(T-T_m)+A_s v \tag{38}$$

$$\frac{\rho}{\varepsilon}\frac{\partial w}{\partial t}+\frac{\rho_f}{\varepsilon^2}\left(\vec{U}\nabla w\right)=-\frac{\partial p}{\partial z}+\frac{\mu_f}{\varepsilon}\nabla^2 w-\left(\frac{\mu_f}{K}+\frac{\rho_f F_1}{\sqrt{K}}|w|\right)w+A_s w \tag{39}$$

In addition, H is the enthalpy of the molten material and is calculated as the sum of sensible enthalpy and latent heat as follows.

$$\mathrm{H}=\mathrm{h}+\Delta\mathrm{H}=\mathrm{h}_{ref}+\int_{T_{ref}}^{T}c_p dT+\beta \mathrm{L}_{sf}$$

β for the melt liquid fraction is defined as follows [48,50].

If $T < T_{solidification}$, β = 0. If $T > T_{liquefaction}$, β = 1.

If $T_{solidification} < T < T_{liquefaction}$ at the interface .$\beta = \frac{T-T_{solid}}{T_{liquid}-T_{solid}}$

The momentum loss due to decreasing porosity in the partially solid region was calculated with Eq. (40) [47].

$$S=\frac{(1-\beta)^2}{(\beta^3+\dot{\varepsilon})}A_{mush}(\vec{v}-\vec{v}_p) \tag{40}$$

Here $\dot{\varepsilon}$ is a very small number (0.001) to avoid division by zero and A_{mush} is the partial solid–liquid region constant and can be taken as approximately 10^4 [51]. The solid velocity is $\vec{v_p}$, If solidified material is not being pulled from the domain, $\vec{v_p}=0$.

The phase change problem was addressed using the finite element method within the ANSYS Fluent environment. As illustrated in Fig. 9a and Fig. 9b, both the flat and finned solar furnace models have identical geometric dimensions: a height of 200 mm and a diameter of 260 mm. For the flat furnace model, a two-dimensional simulation was performed with a structured mesh comprising elements of 2 mm size and a uniform mesh size function. The mesh consisted of 16,509 nodes and 16,255 elements. For the finned furnace model, a three-dimensional simulation was conducted. The mesh element sizes ranged from 1 mm to 5 mm, again with a uniform size function. This mesh structure included 85,980 nodes and 468,279 elements. The mesh quality, quantified by the orthogonal quality metric, was found to be 0.84, indicating good computational stability.

Initial and boundary conditions; Initially, the PCM is in a solid state with a uniform temperature of 300 K. The focal surface is subjected to a constant temperature of 500 K, while the remaining outer surfaces of the furnace are held at 305 K. The furnace structure is made of stainless steel with a thickness of 2 mm, whereas the focal surface is a 0.2 mm thick stainless steel layer. The boundary and initial conditions are defined as follows: At time t = 0 → T = T_i, Constant temperature boundary at the focal surface x = 0, y = *l*, z = 0 → T = T_{foc}, Outer surfaces of the furnace, x = r, y = *l*, z = r → T = T_{wall}, No-slip condition on all wall boundaries, $\vec{U}$=0. Where T_i is PCM initial temperature (K), T_{wall} is the boundary temperature of the furnace (K), r is radius of cylindrical furnace, *l* is length of furnace and t is time.

2.2.3. Experimental setup

The initial and boundary conditions and assumptions regarding the installation of thermal energy storage units for Model-I and Model-II with the RAC system are presented in this section.

2.2.3.1. Experimental determination of focal point temperature. The focal point temperature and simultaneous solar irradiance were experimentally measured in Trabzon, Turkey, during the months of January and July. In the January experiments, the instantaneous solar irradiance incident on the RAC system was recorded to be within the range of 900–1000 W m^{-2} when the solar elevation angle is approximately 45°. According to the manufacturer's specifications, the solar irradiance

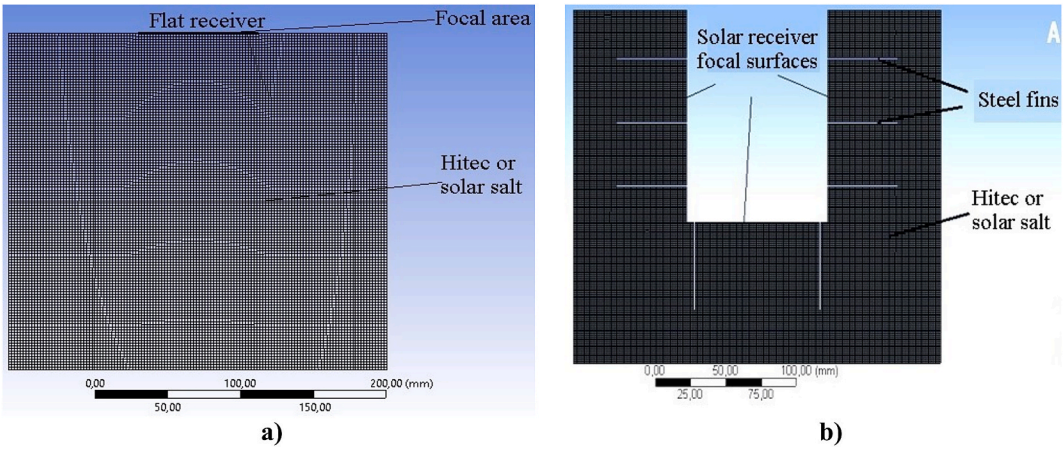

Fig. 9. Mesh structures of PCM in the designed solar furnaces; a) Model-I b) Model-II.

measuring device (Solar Power Meter) had an uncertainty of ± 50 W m^{-2} at an irradiance level of approximately 1000 W m^{-2}. The effective focal spot diameter of the RAC system was measured to be approximately 12 cm, and the average focal point temperature was observed to vary between 520 K and 570 K. Additionally, the digital thermometer and thermocouple sensors used in conjunction with a data logger were factory-calibrated, with a measurement uncertainty of ± 1 K at 373 K.

2.2.3.2. Experimental study for solar salt with Model-I. In the experimental investigation conducted with Model-I, the temperature profile and melting behavior of solar salt inside the furnace were examined under real environmental conditions. The experiment was performed on a clear, sunny day in January 2023. During the test, the ambient temperature was approximately 287 K, with wind speeds ranging between 5–8 km h^{-1} in the east–west direction, and relative humidity around 55 %. Throughout the day, the solar elevation angle in Trabzon varied between 35° and 45°. Focal point temperatures were monitored using two K-type thermocouples, while the temperature of the solar salt and the outer furnace surface were measured using T-type thermocouples. All temperature data were recorded continuously with a data logger for further analysis.

2.2.3.3. Experimental study on Hitec salt with Model-II. In the experimental investigation conducted with Model-II using Hitec salt, temperature measurements inside the furnace were continuously recorded throughout the day using eight thermocouple elements connected to a data logger. The measurements were obtained under solar irradiation levels ranging between 950–1050 W m^{-2}. The experiment took place on a clear, sunny day on July 15, 2024, under ambient conditions of approximately 300 K, a northward wind speed of 5–8 km h^{-1}, and relative humidity around 70 %. A photograph of the newly designed RAC-solar furnace system used in the experimental setup is provided in Fig. 10.

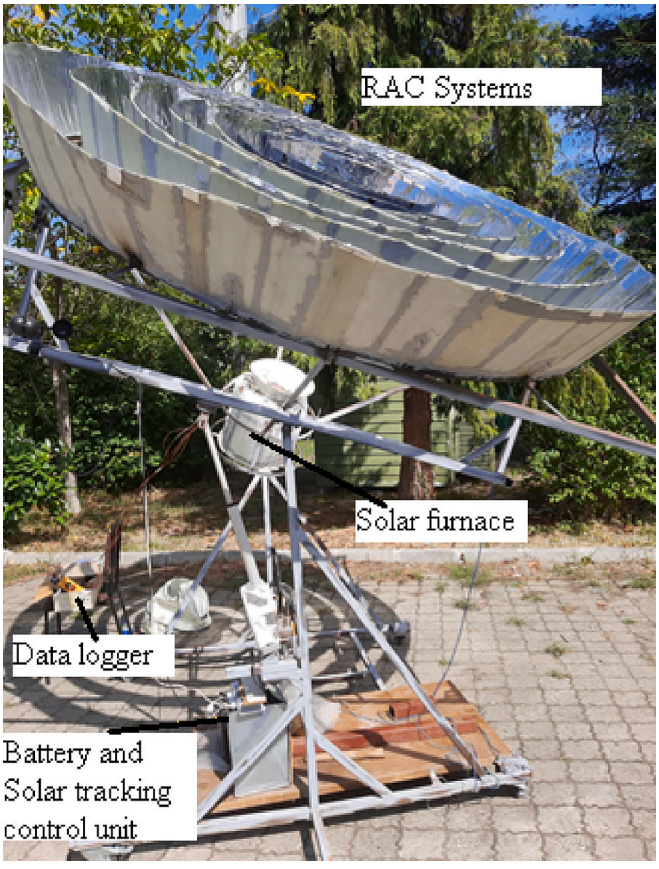

Fig. 10. An experimental image of the new RAC–furnace thermal energy storage system.

3. Results

The results of this study are presented in three categories: analytical, numerical, and experimental.

3.1. Analytical results

Analytical assessments were carried out for both Model-I and Model-II, as detailed below.

3.1.1. Analytical results for Model-I

The optical efficiency of the RAC system is analytically calculated to be 58.8 %. Based on this efficiency, the temperature distribution of the solar salt within the Model-I system was determined. For Model-I, the focal temperature was estimated to be 550 K under ideal solar concentration conditions. As illustrated in Fig. 11. the temperature of the solar salt increased steadily throughout the day, reaching 380 K after 8 h of exposure. At this point, the melting ratio of 24 kg of solar salt was calculated to be approximately 2.8 %. Based on these findings, the average thermal efficiency of the furnace was estimated at 5.5 %. Similarly, when 24 kg of Hitec salt was used in the Model-I system, the salt temperature reached approximately 390 K after 10 h, as shown in Fig. 12. The corresponding melting ratio of the Hitec salt was calculated to be around 16 % by the end of the heating period.

3.1.2. Analytical results for Model-II

In the Model-II, for 18 kg of solar salt, as seen in Fig. 13, if the focal temperature is taken as 500 K, the average salt temperature reached in 10 h is 466 K and approximately 3 kg of salt was melted with a melting rate of 17.7 %. Thus, the mass flow rate for solar salt was determined as 0.0833 g s^{-1}.

In the Model-II, the time until the melting of all 18 kg of Hitec salt, solved using the analytical method, was calculated as approximately 7 h by Eq. (17). Accordingly, analytically the instantaneous melting flow rate is calculated as 0.714 g s^{-1}. Analytically, the average furnace temperature under certain conditions was measured as 448 K, while the furnace thermal energy efficiency was calculated as 28.3 %. The temperature distribution in the furnace at 25200 s is given in Fig. 14.

3.2. Numerical results

The numerical simulation results for Model-I and Model-II are presented as follows.

3.2.1. Numerical results of the Model-I

The numerical analysis for Model-I was performed using ANSYS Fluent, where the focal point temperature was fixed at 550 K above the melting point of solar salt (495 K). As shown in Fig. 15, temperature and melting contours were evaluated over an 8-hours period (28,800 s). By the end of the simulation, only 2.5 % of the solar salt approximately 0.7 kg had melted, indicating that complete melting of 24 kg of salt within a single day is not achievable with this configuration. Fig. 16 presents the time-dependent variation in focal point temperature, average salt temperature, and the corresponding melting rates. Based on these results, the numerical thermal efficiency of the Model-I furnace was calculated as 4.6 %, using Eq. (23).

In numerical modeling, for Hitec salt in a 24 kg in the Model-I, 4 kg of salt was melted in 10 h with an average salt temperature of 369 K and a melting rate of 16.7 %. In Fig. 17a shows the variation of the melting rate of Hitec salt with time in Model-I. The variation of Hitec salt temperature with time in the Model-I is given in Fig. 17b.

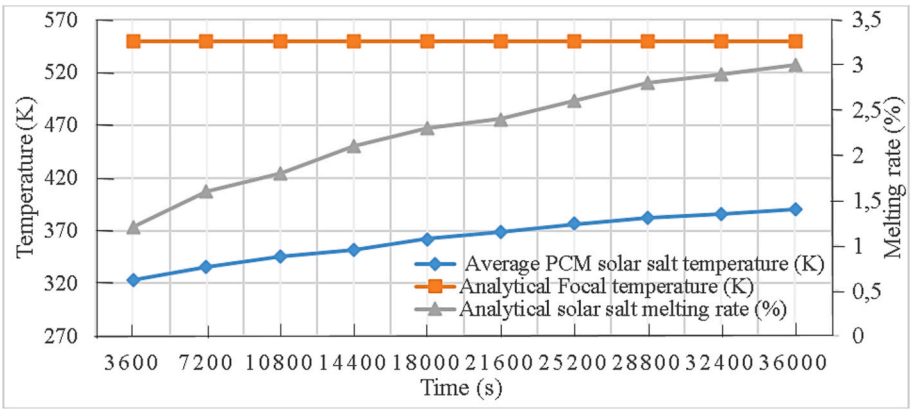

Fig. 11. Variation of solar salt temperature and melting rate with time for Model-I.

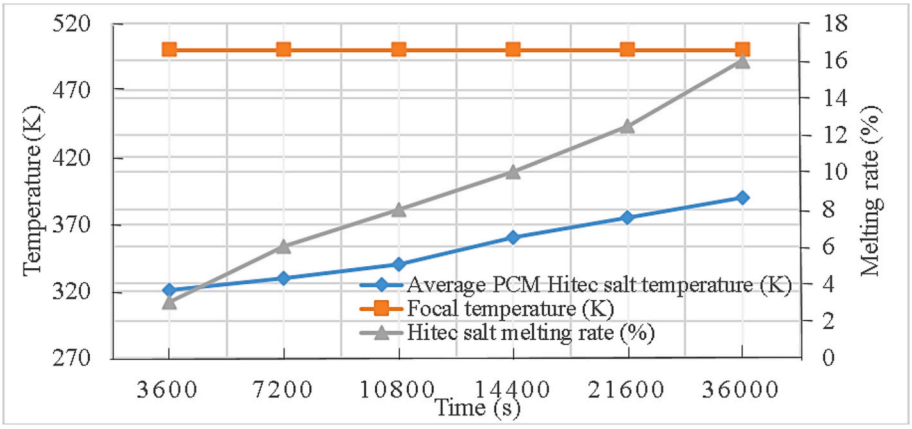

Fig. 12. Variation of Hitec salt temperature and melting rate with time for the Model-I.

3.2.2. *Numerical results for Model-II*

The numerical performance of the RAC-finned solar furnace (Model-II) was analyzed using both solar salt and Hitec salt as PCMs. Model-II was specifically designed to overcome the prolonged melting duration observed in Model-I by enhancing heat transfer through extended surface area via fins, thereby accelerating the phase change process. For solar salt, numerical simulations were conducted with 18 kg of material. After 10 h, approximately 3.2 kg of salt had melted, corresponding to a melting rate of 17.6 %, with an average temperature of 462 K. As illustrated in the Fig. 18, the melting rate increased steadily during the initial 10,000 s, after which the melting process began to slow down. This reduction in melting rate is attributed to the decreasing heat conduction in regions farther from the fins, due to the relatively low thermal conductivity of solar salt. Additionally, Fig. 19 presents the (a) melting and (b) temperature contours of the solar salt at the end of the 10-hours simulation. These results clearly indicate that complete melting of the solar salt could not be achieved within a single day under the given thermal conditions. Consequently, to evaluate the system under improved thermal conductivity and melting characteristics, a second simulation was conducted using Hitec salt. The physical properties of Hitec salt were implemented into the ANSYS Fluent environment based on literature data. A focal temperature of 500 K, calculated analytically, was applied as a boundary condition for the simulation.

As shown in Fig. 20, for Model-II, when the focal receiver surface is maintained at 500 K, the average heat flux on the receiver surface in the second hours is found to be between 10,500–12,000 W m^{-2}. This result

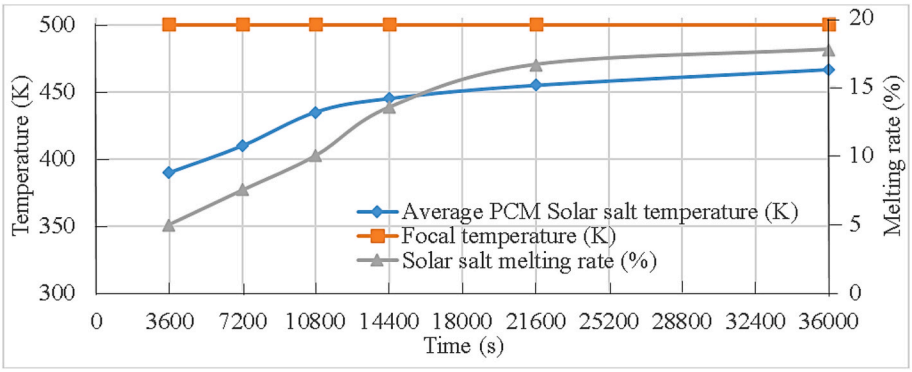

Fig. 13. Variation of focal, solar salt temperature and melting rate with time for Model-II.

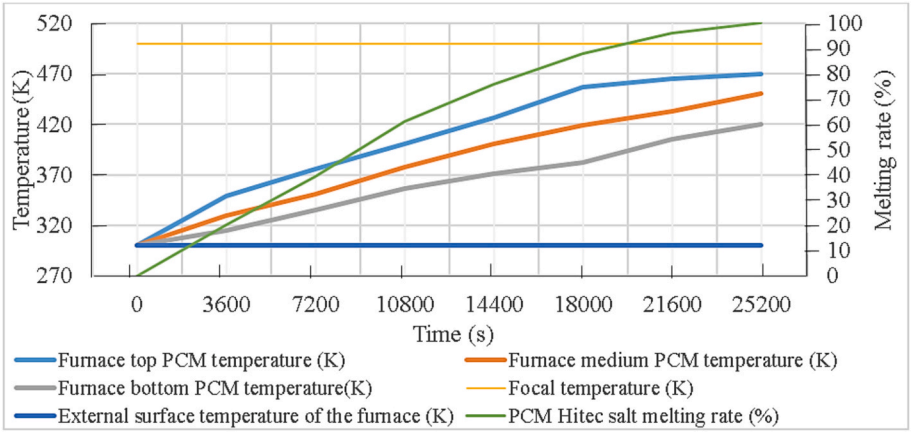

Fig. 14. Variation of Hitec salt temperature and melting rate with time for Model-II.

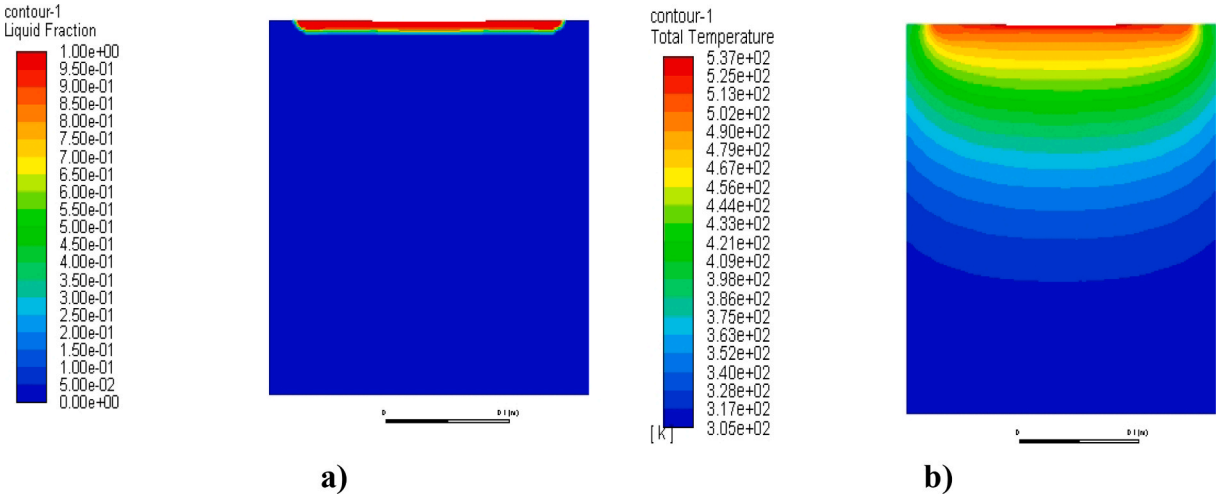

Fig. 15. In Model-I for solar salt at 28800 s; a) Melting and b) Temperature contours.

closely aligns with the analytically calculated heat flux value. In addition, the heat transfer coefficient at the focal surface was obtained between 20–50 W $m^{-2}K^{-1}$ by numerical method.

Fig. 21 shows the melting contours of inorganic Hitec salt at 3600 s, 7200 s, 14400 s and 25200 s, respectively. In this case, as seen in the graph, the addition of cylindrical fins to the solar furnace doubled the surface area and shortened the phase change period. Additionally, in Fig. 21d, it can be seen that approximately 18 kg of Hitec salt completely melted in 25200 s.

Fig. 22 shows the temperature contours on the Hitec salt in Model-II. Numerically, at the 25200 s, the average focal temperature reached 500 K and liquid melt the average temperature was obtained as 455 K.

Fig. 23 shows the variation of the melting rate of Hitec salt with time for the Model-II. It seems that the melting rate of the Hitec salt occurs rapidly, up to approximately 10800 s, and approximately 65 % of it is melted. In the remaining 35 % of the melting, the melting rate slowed down and the melting is completed in approximately 25200 s.

According to the CFD analysis results in the Fluent of the Model-II,

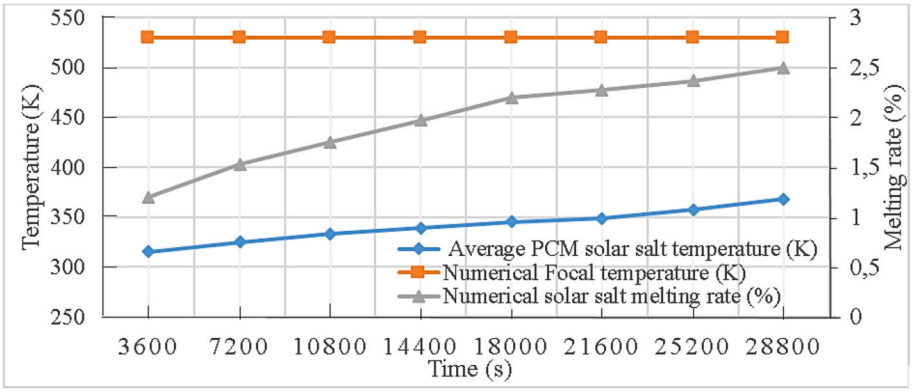

Fig. 16. Variations of solar salt temperature and melting values with time in Model-I.

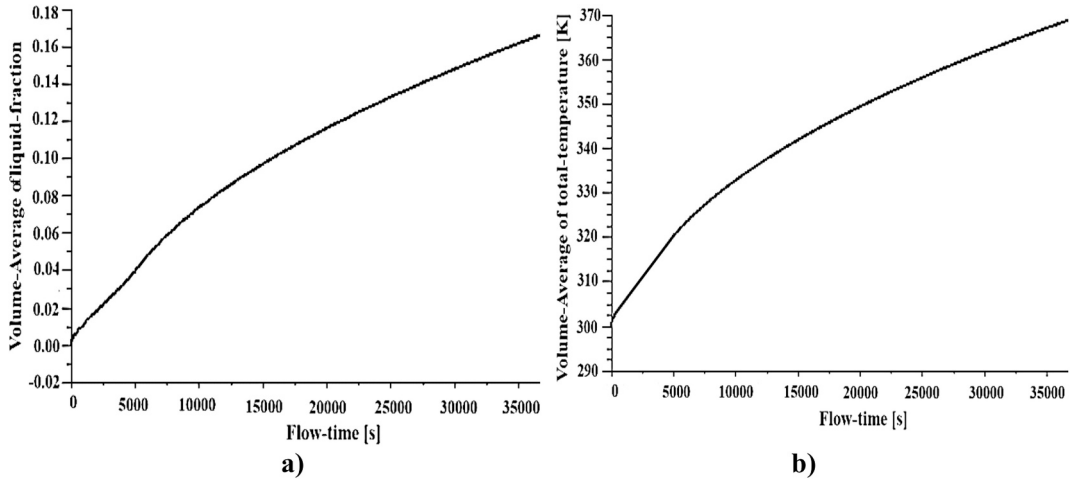

Fig. 17. Variations liquid fraction (a) and temperature (b) of Hitec salt with time in Model-I.

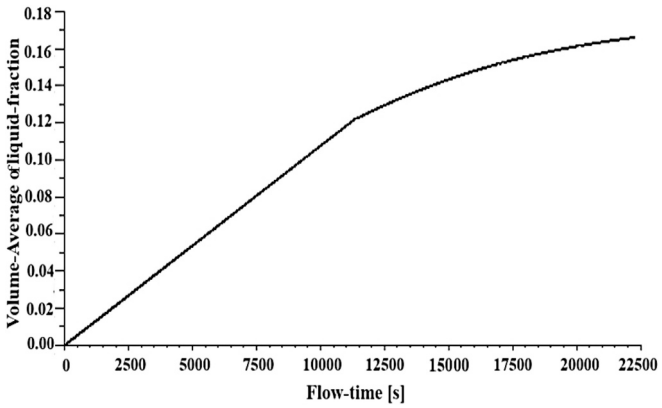

Fig. 18. Variation of solar salt melting rate with time for Model-II.

thermal energy efficiency of the furnace is calculated as 17.5 % with Eq. (23) when all the Hitec salt was melted. The average Hitec salt temperature at this moment is obtained as approximately 455 K. Numerically and analytically, the total melting time of the Hitec salt is very close to each other and is approximately 7 h.

3.3. Experimental results

Experimental data performed with Model-I and Model-II are presented in this section. In addition, measurement errors and uncertainty rates in the experiments are determined and verified with numerical methods.

3.3.1. Experimental results of Model I

In this experiment, the average focal point temperature was measured as (570 ± 25) K when the average solar radiation during the day was 1035 W m^{-2}. In addition, it was observed that the temperature measured on the solar salt in the Model-1 reached a maximum of 378 K. Since the furnace interior temperature was lower than the melting point of solar salt (495 K), melting occurred only in the focal area.

In addition, Fig. 24 shows the focal and furnace solar salt temperature changes according to the solar intensity throughout the day in the experiment carry out with Model-I. According to these experimental data, the average thermal energy efficiency of the furnace is calculated as 6 % with Eq. (23).

3.3.2. Experimental results of Model-II

In the experimental study carry out with Model-II, the temperature values in the furnace measured throughout the day in the range of

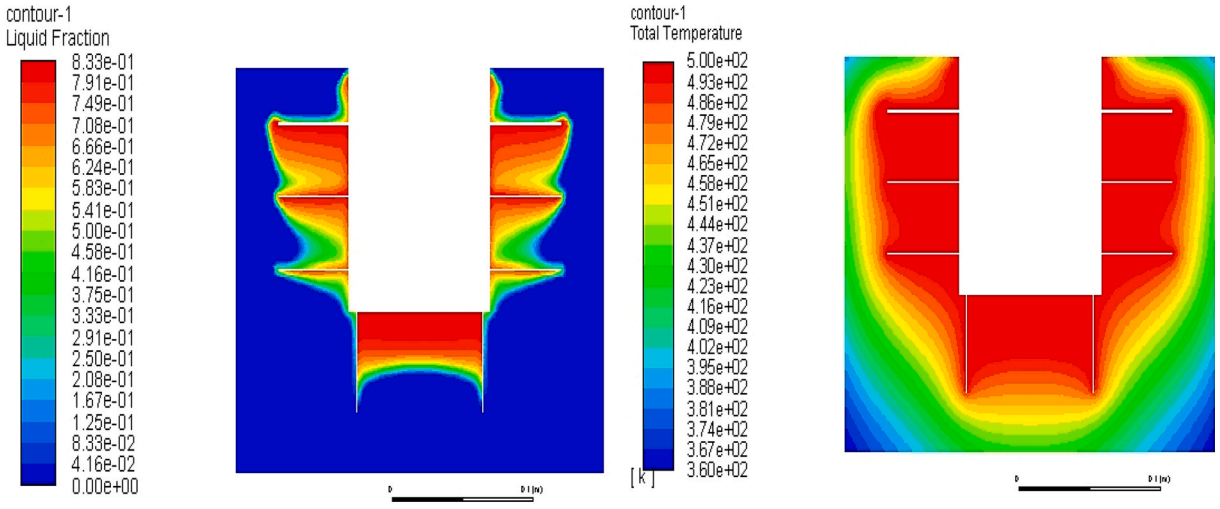

Fig. 19. A) melting and b) temperature contours of solar salt in model-ii.

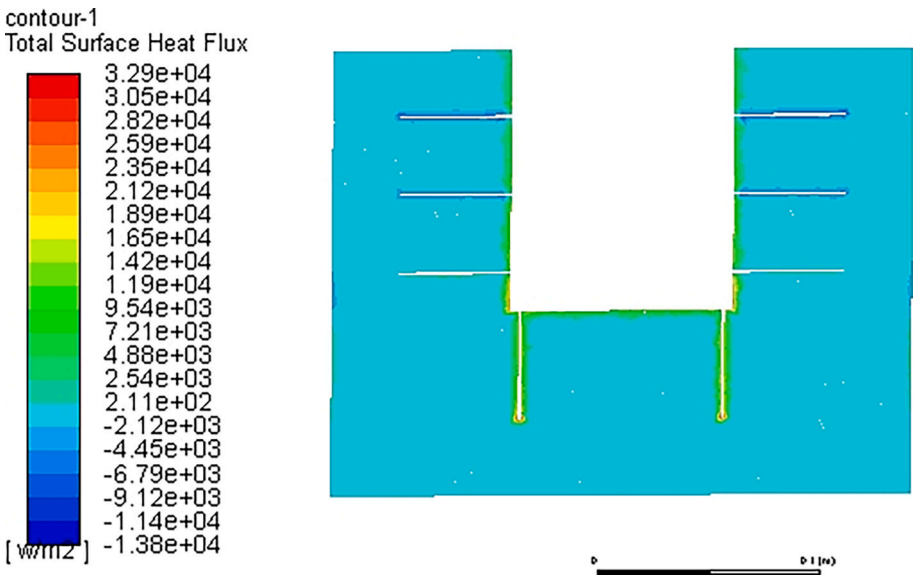

Fig. 20. Heat flux contour of the receiver surface for Model–II.

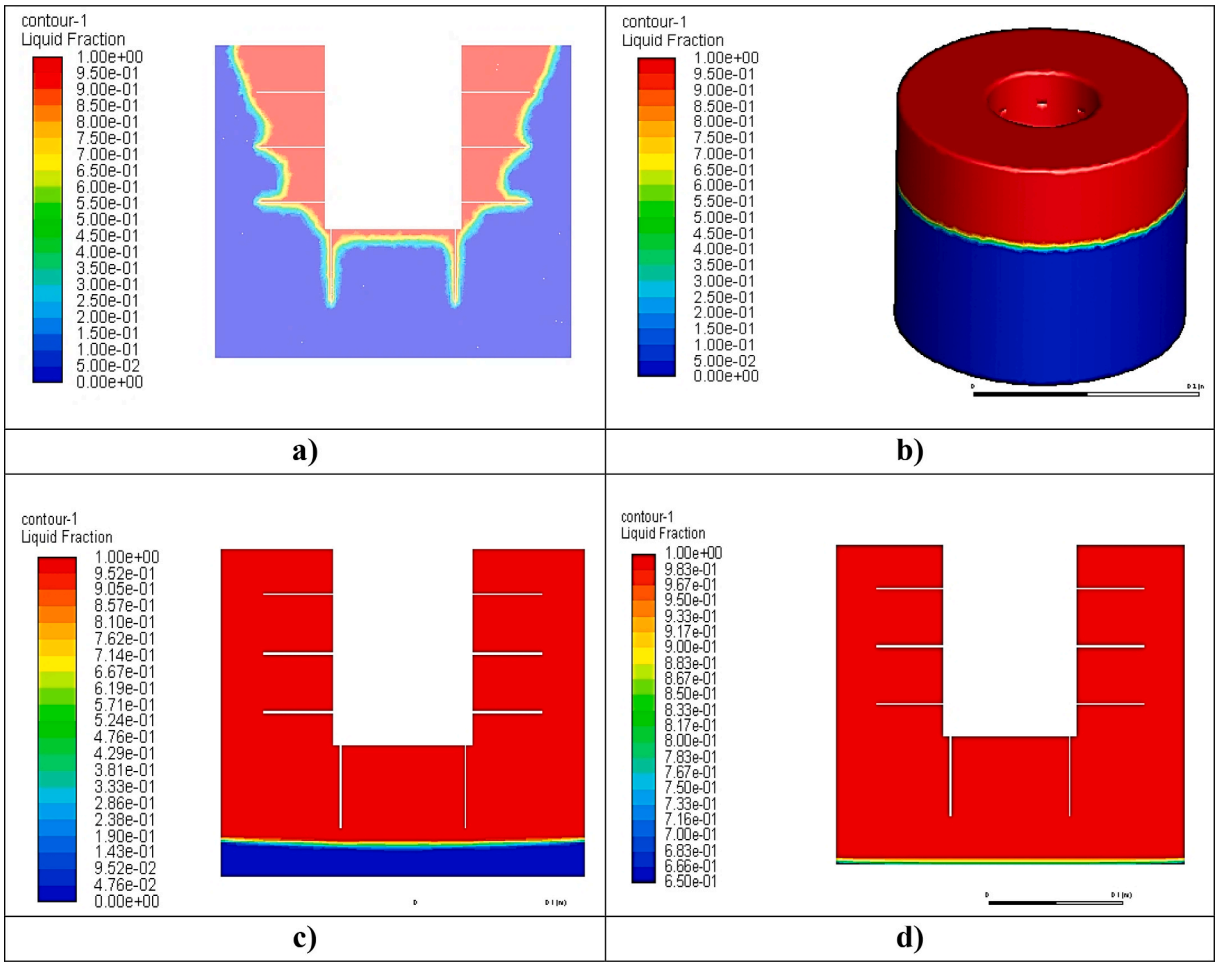

Fig. 21. Melting contours of Hitec salt in Model-II at a) 3600 s, b) 7200 s, c) 14400 s and d) 25,200 s

900–1020 W m^{-2} of the solar radiation value are given in Fig. 25. When this figure is examined, the focal temperature values are approximately in the range of 475–565 K. At the end of the seven-hour experiment carry out in July, the Hitec salt in the solar furnace was melted and the average furnace temperature was measured to be approximately 440 K. In this experiment, the melting flow rate of Hitec salt was found to be 0.72 g s^{-1}. In addition, the thermal energy efficiency of the furnace is calculated experimentally as 22.11 % with Eq. (23) and the exergy

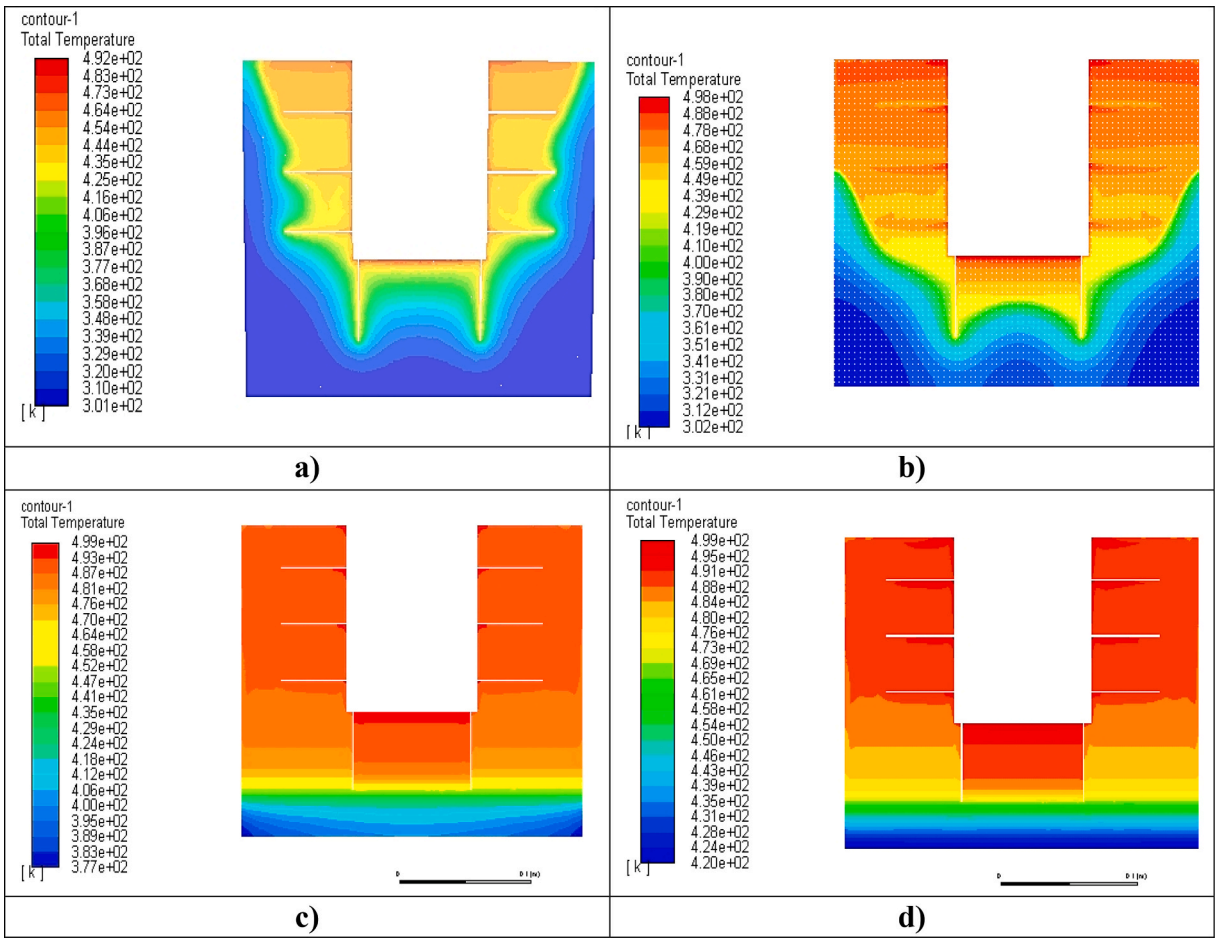

Fig. 22. Temperature contours of Hitec salt in Model-II at a) 3600 s, b) 7200 s, c) 14400 s and d) 25200 s.

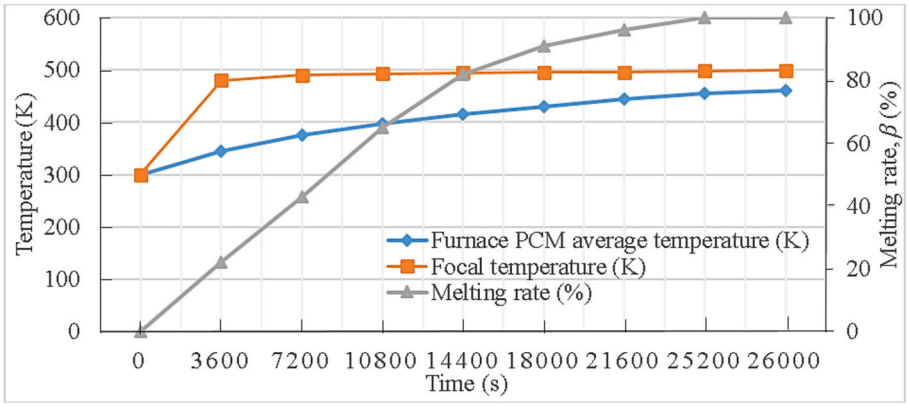

Fig. 23. Variation of melting rate and average temperature with time of Hitec salt in Model-II.

efficiency is calculated as approximately 11.5 % with Eq. (32) depending on the melt mass flow rate. While melting occurs faster in areas where concentrated solar energy is directly applied, the melting rate towards the bottom of the furnace is slower due to the low heat conduction coefficient of Hitec salt.

3.3.3. *Comparison of experiments in different seasonal conditions*

In January, solar radiation ranged from 860 to 980 W m^{-2}, with focal temperatures between 520 and 560 K. The average temperature of the Hitec salt inside the furnace varied from 320 to 418 K, while ambient temperature, wind speed, and humidity were recorded as 283–287 K, 5–8 km h^{-1}, and 42–52 %, respectively. Under these conditions, the furnace achieved an average thermal efficiency of 16 % throughout the day. During July, solar radiation increased to 950–1050 W m^{-2}, with focal temperatures ranging from 460 to 540 K. The average Hitec salt temperature inside the furnace rose to between 345 and 445 K, with ambient temperature at 297–300 K, wind speeds of 5–7 km h^{-1}, and humidity levels between 60 and 70 %. Consequently, the average daily thermal efficiency improved to 23 %. A comparison of furnace temperature and thermal efficiency between winter and summer conditions is illustrated in Fig. 26. Due to the sun-tracking capability of the system, solar rays consistently impinge perpendicularly on the concentrator,

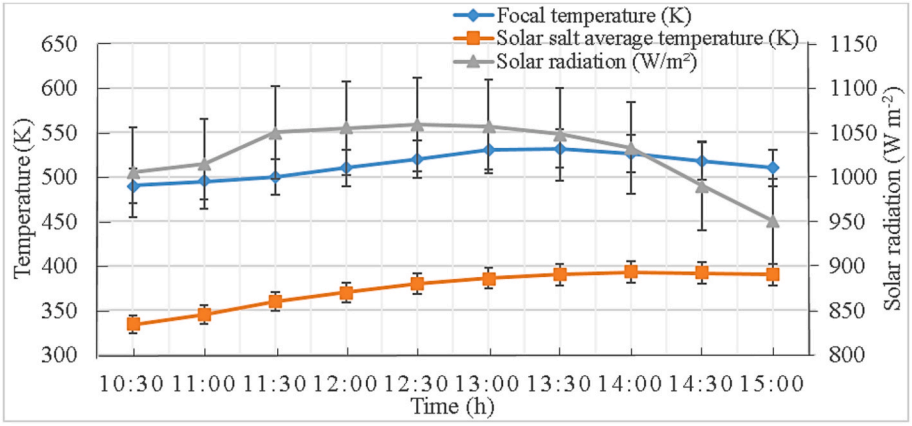

Fig. 24. Change of solar intensity and furnace temperatures in the Model-I during the day.

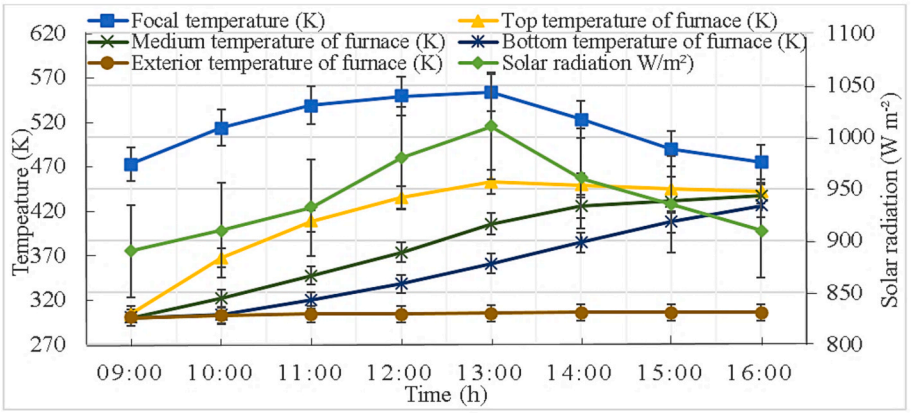

Fig. 25. Changes of solar intensity and Hitec salt temperatures in the Model-II during the day.

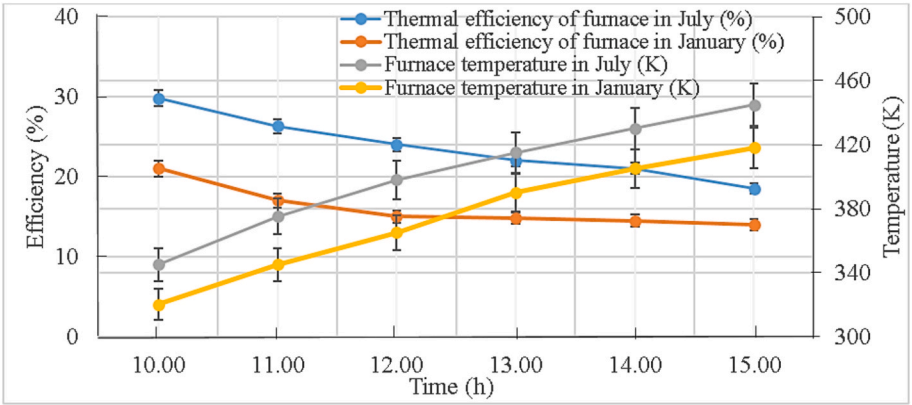

Fig. 26. Temperature and efficiency relationship of RAC-furnace system in different seasons.

minimizing periodic fluctuations in solar radiation. When the furnace is well-insulated, variations in ambient temperature have a minimal impact on the internal temperature. However, sudden increases in wind speed exceeding 9 km h^{-1} result in noticeable drops in focal temperature. Therefore, the designed system performs optimally under clear, sunny conditions with wind speeds below 8 km h^{-1}. Additionally, higher humidity levels reduce air clarity, leading to a decrease in total global solar radiation.

Following the experiment conducted in January, the discharge process of Hitec salt was evaluated using the Model-II furnace. The temporal variations in temperature within the furnace during this process are presented in Fig. 27. Despite the ambient temperature being approximately 286 K, the lack of insulation at the furnace's top focal area led to a more rapid temperature decline in that region. In contrast, due to insulation around the rest of the furnace, temperature decrease was slower, particularly in the lower sections. During the discharge period, the average furnace temperature dropped to 327 K within approximately 4 h. These findings indicate that the system, after being charged for roughly 7 h during the day, is capable of storing thermal energy—both latent and sensible—for a total duration of around 11 h including the discharge phase.

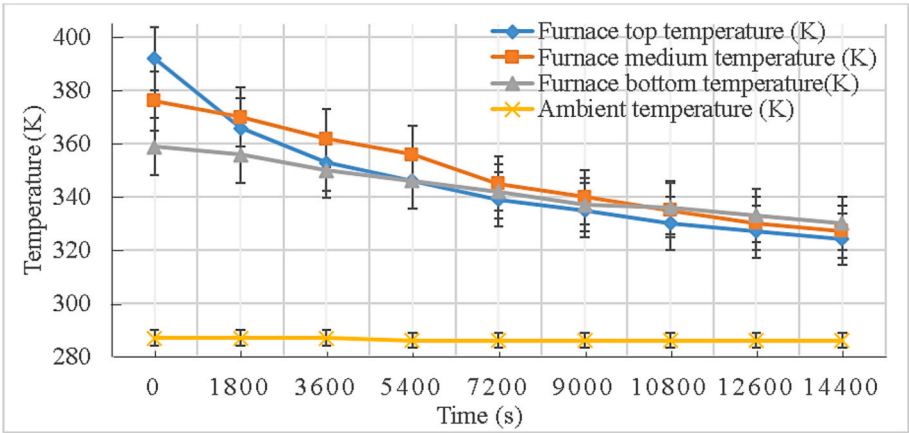

Fig. 27. Temperature variation with time during discharge process of Hitec salt with Model-II in January.

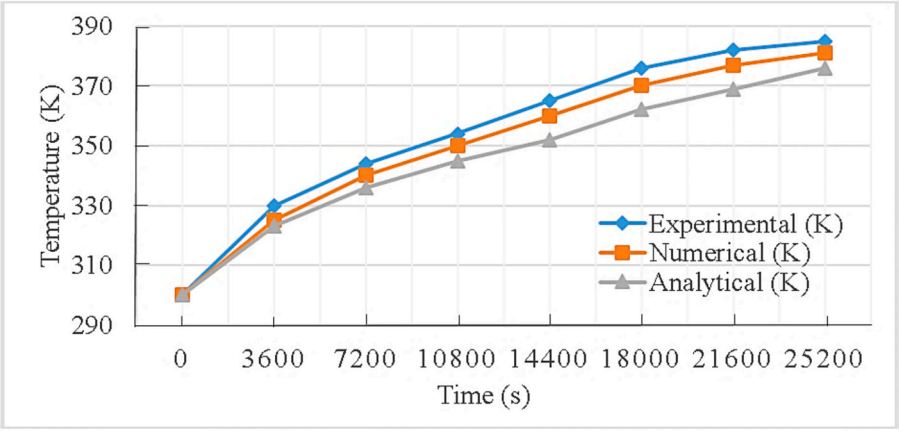

Fig. 28. Temperature variations of solar salt with time according to all methods with Model 1.

3.3.4. Error and uncertainty analyses of Ring Array concentrator and solar furnace

Error analysis was conducted to quantify the inaccuracies arising from measurements and modeling during the experiments. Additionally, uncertainty analysis was employed to estimate the reliability of the optical efficiency uncertainty is estimated at 5 %. The overall uncertainty in the thermal efficiency calculation was derived using the Gauss uncertainty propagation method by taking partial derivatives of the efficiency with respect to relevant parameters, as expressed in Eq. (41).

$$u_{\eta=}\sqrt{\left(\frac{\partial\eta}{\partial\dot{m}}u_{\dot{m}}\right)^2+\left(\frac{\partial\eta}{\partial cp}u_{cp}\right)^2+\left(\frac{\partial\eta}{\partial T}u_T\right)^2+\left(\frac{\partial\eta}{\partial I}u_I\right)^2+\left(\frac{\partial\eta}{\partial A}u_A\right)^2+\left(\frac{\partial\eta}{\partial\eta_{op}}u_{\eta_{op}}\right)^2+\left(\frac{\partial\eta}{\partial\alpha_r}u_{\alpha_r}\right)^2} \tag{41}$$

measured and calculated values. The measurement errors associated with the RAC and solar furnace include systematic, random, and modeling uncertainties. Experimentally determined error margins are as follows: thermocouple ±% 0.75 °C, digital thermometer ±% 0.5 °C, solarimeter ±% 5 W m^{-2}, ray sensor of solar tracking system ±% 1.1, incident solar beam angle ± 2.2 %, focal temperature measurement ±% 5 °C, internal furnace temperature measurement ±% 3 °C, concentrator total surface area measurement ±% 2.8 m^2, optical reflection ±% 3, receiver absorption ratio ±% 5 and flow measurement ±% 5 kg s^{-1}.

Using the combined uncertainty method proposed by Kline and McClintock [52], the total absolute uncertainty in solar irradiance measurement is approximately 5.1 %. The internal furnace temperature measurement carries a total absolute uncertainty of 3 %, while the For each experimental hour, the total uncertainty for thermal efficiency is evaluated using Eq. (23), while the uncertainty in exergy efficiency is calculated using Eq. (32). Key parameters influencing the accuracy include mass flow rate ($\dot{m}$), specific heat (c_p), furnace temperatures (T), solar radiation (I), optical efficiency (η_{op}), concentrator surface area (A_{RAC}) and receiver absorption coefficient (α_r). The calculated uncertainty in thermal efficiency is ∓ 0.034 and corresponding to a relative uncertainty of (u/η_{fur}) 14.7 %. For exergy efficiency, the uncertainty (u/ψ_{Fur}) is ∓ 0.013 with relative uncertainty is 11.38 %. These uncertainty levels are considered acceptable and demonstrate sufficient measurement precision for the study.

3.3.5. Verification of numerical results with experimental results

This section presents the validation of theoretical predictions against experimental results for both Model-I and Model-II. Firstly, the temporal

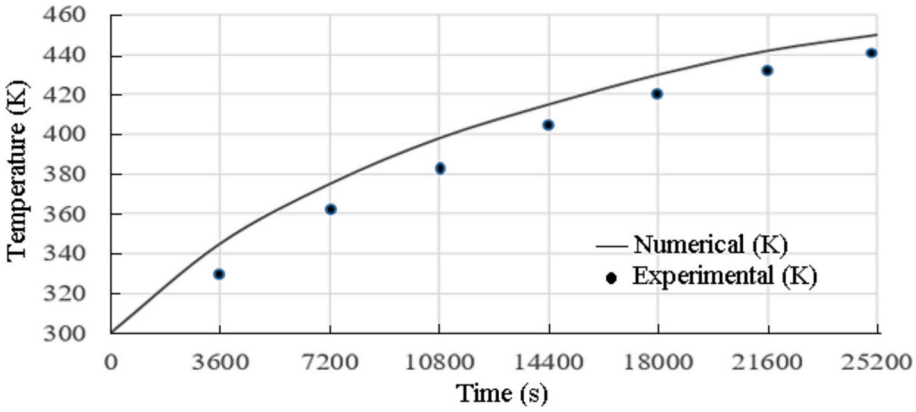

Fig. 29. Numerical and experimental comparison of Hitec salt temperatures for Model-II.

variation of solar salt temperature within the furnace for Model-I is illustrated in Fig. 28. The graph demonstrates a steady increase in the average solar salt temperature over time. Considering the experimental errors and uncertainties, the experimental results exhibit a trend that closely aligns with both the analytical and numerical predictions.

Secondly, during the seven-hour experimental campaign with Model-II, the average furnace temperature was measured at 435 K, as shown in Fig. 29. In comparison, the numerical simulation yielded an average temperature of 450 K. The numerical temperature progression parallels the experimental data, confirming the model's accuracy. Furthermore, it was observed that Model-II achieves higher PCM temperatures than those recorded in Model-I experiments, indicating improved thermal performance in the finned design.

There may be slight discrepancies between the experimental and numerical results. These differences arise primarily because the numerical simulations assume a constant average focal temperature and uniform outer furnace surface conditions throughout the day. In contrast, the actual experimental setup is subject to temporal variations in focal temperature due to fluctuating solar radiation and heat losses by radiation and convection to the ambient environment. To enhance the thermal energy input in future experiments, it is recommended to improve the thermal insulation of the furnace and to utilize a metallic receiver at the focal point with high corrosion resistance and superior thermal conductivity.

4. Discussions

This section presents a comparative evaluation of the analytical, numerical, and experimental results related to internal temperature variations, phase change (melting) rates, and thermal efficiencies of the solar furnace systems. Furthermore, the performance of the newly developed RAC-furnace (Model-II) system is compared with conventional CSP technologies reported in the literature, highlighting its potential advantages in terms of heat storage performance and system efficiency.

4.1. Comparison of analytical, numerical and experimental data

Based on both experimental and theoretical investigations, it was observed that the melting process of high-volume inorganic salts progresses relatively slowly in the Model-I furnace due to limited heat transfer. In contrast, the Model-II furnace featuring an internally finned cylindrical receiver with top-applied heat facilitates enhanced heat distribution, resulting in higher melting rates and elevated internal temperatures. For Hitec salt, the average mass flow rates are calculated as 0.1113 g s^{-1} in Model-I and 0.72 g s^{-1} in Model-II. Similarly, for solar salt, the mass flow rates are determined as 0.024 g s^{-1} and 0.0877 g s^{-1}, respectively. The superior melting rate of Hitec salt in both furnaces implies a greater latent heat storage capacity. Furthermore, the incorporation of internal fins in Model-II significantly improved heat transfer within the PCM domain, enhancing thermal storage efficiency. These findings demonstrate the effectiveness of Model-II when paired with Hitec salt for thermal energy storage applications.

As illustrated in Fig. 30, the temporal variation of Hitec salt temperature in Model-II is presented for analytical, numerical, and experimental results. The trends show good agreement across all methods, with a consistent increase in salt temperature over time, validating the reliability of the modeling approaches used in this study.

In Fig. 31 shows that the liquid fractions of Hitec salt melted in the Model-II with numerically, analytically and experimental. In analytical and numerical methods, the melting rates after two hours were 39.5 % and 43 %, respectively. In the experiments, analytical and numerical

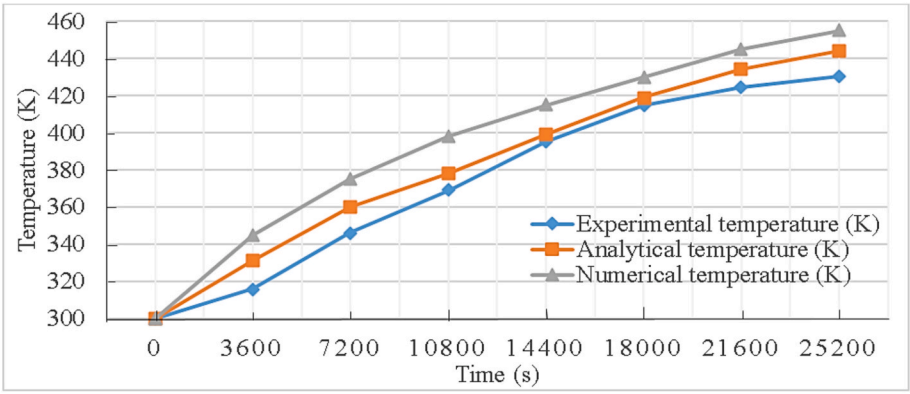

Fig. 30. Experimental, numerical and analytical comparison of Hitec salt temperatures in the Model-II.

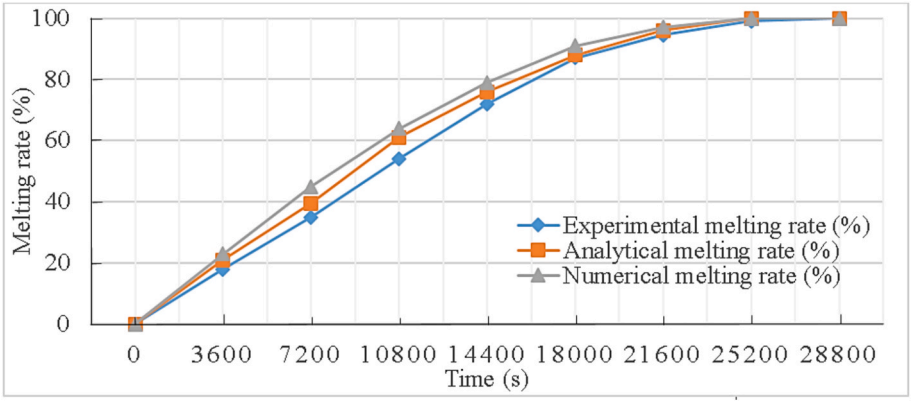

Fig. 31. Experimental, numerical and analytical comparison of melting rates of Hitec salt.

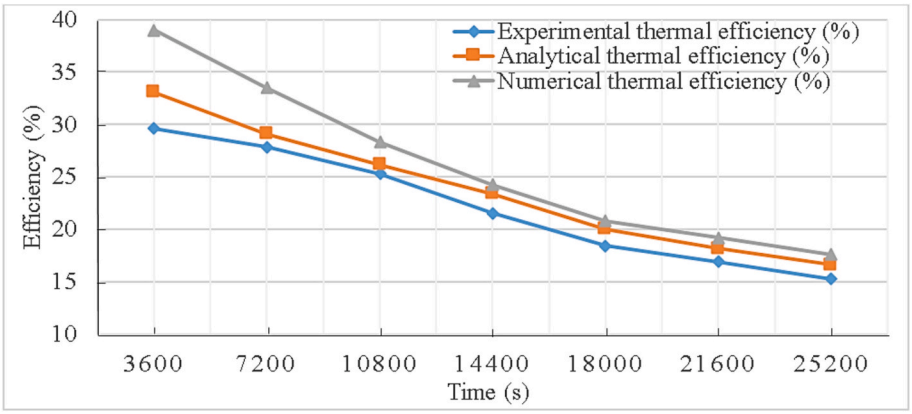

Fig. 32. Comparison of numerical, analytical and experimentally calculated furnace thermal energy efficiencies.

methods, it can be seen in the graph that the melting rates approach each other and completely melt in seven hours. Melting flow rates were calculated according to the amount of PCM liquid melted in depending on time the Model-II. In each method, while the melting flow rate was higher in the first hours, the melting flow rate decreased after the fourth hour. The reason for the decrease in melting flow rate is the slowdown of heat conduction towards the bottom of the furnace.

When Fig. 32 is examined, it is seen that the furnace efficiency decreases with time in all methods. The reason for this situation is that the melting flow rate decreases over time in the furnace. In experiments, analytical and numerical average furnace thermal efficiencies are calculated with Eq. (23) as 23 %, 23.8 % and 26 %, respectively. It is seen that the furnace efficiencies are close to each other. The average exergy efficiencies of the RAC-furnace system are calculated numerically and experimentally as 12.4 % and 11.5 %, respectively with Eq. (32). Additionally, the total thermal and total exergy efficiencies of the RAC-furnace system containing Hitec salt are calculated as 11 % and 6.2 % with Eqs. (33) and (34), respectively.

Analytically, the average thermal energy and exergy efficiencies of the RAC system were calculated as 58.6 % and 35.4 % with Eqs. (20) and (21), respectively. As the concentration rate increases, the focal temperature increases. Exergy losses and destruction of the RAC system were calculated as 1898 W with low concentration ratios. Exergy loss and exergy destruction of the Model-II were calculated as 668 W on

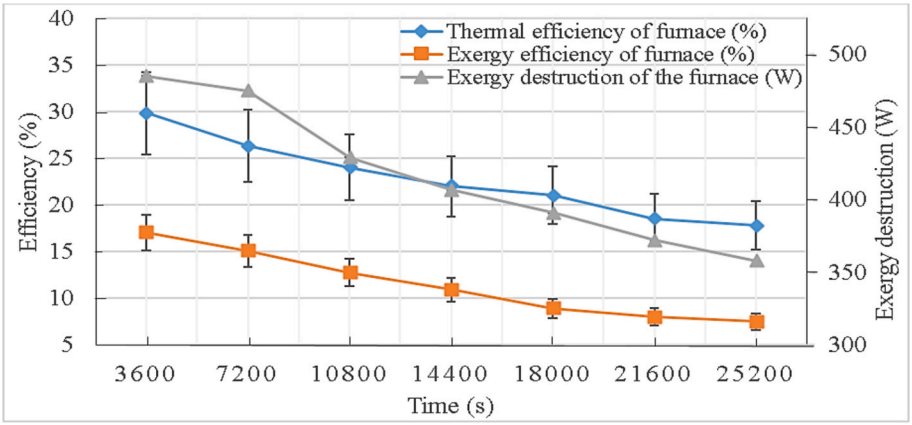

Fig. 33. Temporal variation of experimental thermal and exergy efficiencies (including error bars) and exergy destruction for Model-II.

average. In this case, the average exergy loss from the cylindrical focal surface of the Model-II is 255 W. Entropy production decreased as the average temperature in the solar furnace increased. It was also revealed that the exergy loss of RAC is greater than that of the solar furnace. In order to increase the thermal energy coming into the furnace, it is necessary to increase the optical efficiency of the RAC system by optimizing the concentrator assembly and eliminating the surface roughness. The time-dependent variations of thermal energy and exergy efficiency including the error rates and exergy destruction of Model-II, are given in Fig. 33. Accordingly, exergy destruction decreased with time and was calculated as 358 W at the end of 7 h. Additionally, while the error bars are presented on the thermal and exergy efficiency, the uncertainty rate for the thermal efficiency of the furnace is 14.7 %, while the uncertainty rate for the exergy efficiency is 11.3 %.

4.2. Comparison of the system with concentrated solar power systems in the literature

The comparison of the RAC system types with similar designs in the literature is presented in Table 6. In the numerical study by Garcia et al., with 3.14 m^2 RAC system and a receiver size of 11 mm diameter at the focal point, the concentration ratio was 30960, the focal point temperature was 3300 K, and the optical efficiency was 51 %. The receiver efficiency defined as $(\eta_{rec,lit} = 1 - \frac{\sigma\left(T_{foc}^4\right)}{IC_R})$ in this literature was 78.2 %, and the receiver total conversion efficiency was numerically 35.9 % [5]. However, in the literature, the absorption and emission coefficients were taken as 1 in the receiver efficiency equation. In contrast, in this study, both theoretical and experimental studies were presented for a larger focal diameter of 120 mm. Furthermore, when the maximum focal temperature was 760 K, the receiver efficiency was calculated as 78.9 % with $\eta_{rec,\ lit}$, close to the literature value, while the receiver efficiency was calculated as 64.3 % using Eq. (6). As a result of this situation, it is revealed that if the concentration ratio of the designed RAC system was increased, the receiver temperatures also increased.

In an experimental study by Ky et al., 1.692 m^2 RAC system for cooking was reported to have an average geometric concentration ratio of 38 and a maximum temperature of 603 K for a sunflower oil liquid receiver, with a receiver efficiency of 80 % and a thermal efficiency of 40 %, the product of the receiver and Carnot efficiencies [7]. The receiver efficiencies are close to the literature, but here the absorption and emission coefficients are taken as 1. In addition, optical efficiency analysis and exergy analysis of this RAC system have not been performed.

The experimental study conducted by Mahfuz et al. with the parabolic trough concentrator is compared in terms of energy and exergy efficiency analysis in this table. In their thermodynamic analysis of heat storage applications using a parabolic trough solar collector and a PCM containing H250, they found a concentrator optical efficiency of 45.7 %, a total thermal energy conversion efficiency of 13.5 % for the receiver, and a total exergy efficiency of 9.25 % [53]. However, using the receiver efficiency of Eq. (6), a total thermal energy conversion efficiency of 22.8 % is achieved and also a total exergy efficiency of 7.5 % is obtained for the RAC and solar furnace. H250 PCM has a higher specific heat than Hitec or solar salts. However, in terms of safety and cost, the use of solar or Hitec salts is safer and more economical.

Finally, in the literature, Turrini et al. tested thermal energy storage in two hot and cold tanks using molten Hitec salt as the heat transfer fluid in a 5 m diameter parabolic dish collector and a helical copper tube receiver at the center [54]. In parabolic dish systems, the receiver is positioned opposite the receiver in the RAC system. Therefore, the RAC system has been found to be more suitable for direct heat storage in larger volumes. In addition, using Hitec salt as the heat transfer fluid continuously, as reported in the literature, results in continuous heating due to the solidification of the salt in the pump and the pipe. Therefore, in future studies, the use of thermal oils as heat transfer fluids to transfer the thermal energy stored in the furnace through a heat exchanger is recommended. Furthermore, since copper pipes corrode more rapidly with molten salts, it is more appropriate to choose stainless steel metals

Table 7
Component and total cost values of the RAC-Furnace system.

Product/material/process	Unit price [$]	Total price [$]
Furnace (304 stainless steel)	75	75
3D printer material	30	150
Reflective foil	8	88
Fiberglass	3	30
Epoxy resin	20	200
Battery	70	70
Sodium Nitrate	2.5	62,5
Potassium Nitrate	3	75
Sodium Nitrite	2.5	62,5
Two-axis sun tracking system	250	250
Consumables and labor	300	300
Total		1363 $

Table 6
Comparison of literature and presented RAC systems.

Parameters and subsystems	Garcia et al. [5]	Ky et al. [7]	Mahfuz et al., [53]	RAC-solar furnace (this paper)
Methods	Numerical	Experimental	Experimental	Experimental
Type /Model	RAC	RAC	Parabolic trough	RAC
Installed capacity (W)	3140	1692	250,000	3500
Max focal temperature (K)	3300	603	538	760
Concentration rate C_R	30,962	38	14	90
Receiver efficiency (%),$\eta_{rec,lit}$	78.2	80	67	78.9 64.3 with Eq. (6)
Optical efficiency (%)	51	–	45.7	58.8
Carnot efficiency (%)	90	50.2	44.2	60.5
Thermal efficiency of receiver (%), $(\eta_{rec,\ lit}\ \eta_{Carnot})$	70.3	40	29.6	47.7 38.9 with Eq. (6)
Total thermal conversion efficiency of receiver (%), $(\eta_{op} * \eta_{rec} * \eta_{Carnot})$	35.9	–	13.5	28 22.8 with Eq. (6)
Total exergy efficiency (%), $(\psi_{op} * \psi_{fur})$	–	–	9.25	7.5 with Eq. (32)

with high corrosion resistance as the molten salt medium.

4.3. Economic analyses of ring array concentrator and solar furnace system

The estimated manufacturing costs for the proposed low-cost RAC-furnace thermal energy storage system are presented in Table 7. In the current literature, the average installation costs for commercial CSP systems such as Solar Power Tower and Linear Fresnel Reflector technologies range between $3–11 per watt [55]. In contrast, the installation cost of the developed RAC system was calculated to be approximately $1.4 per watt, highlighting its economic viability for scalable applications. This estimate does not include operation and maintenance (O&M) costs; however, these are expected to be minimal due to the system's simple design and low energy requirements. The RAC-furnace system can be operated via a 12-volt battery used for solar tracking, or directly through a grid connection. Furthermore, integration with a solar panel can render the system completely off-grid, further enhancing its sustainability and reducing long-term operational costs.

For Thermoeconomic analysis, the energy loss ratio ($\dot{E}_L/Z_c$) was determined by the ratio of the thermodynamic energy loss ($\dot{E}_L$) of the entire system to the installation cost of the RAC-furnace heat storage system (Z_c). In addition, the exergy loss ratio was defined as the ratio of the exergy loss of the entire system to the installation cost [56]. According to the experimental and numerical data, the energy loss ratio was calculated as approximately 1.6 W/$ and the exergy loss ratio as 1.95 W/$. As a result, the efficiency of the system can be increased by decreasing the loss rates of the system by increasing the optical efficiency of the concentrator, where the highest loss occurs experimentally.

5. Conclusions

This study investigated a novel RAC-based solar furnace for high-temperature thermal energy storage using inorganic PCMs. The optical performance, temperature distribution, and thermal efficiency of the system were evaluated through analytical, numerical, and experimental approaches.

The performance comparison between two solar furnace configurations Model-I flat receiver and Model-II finned receiver demonstrated significant improvements in heat storage efficiency with the latter. The transition from solar salt to Hitec salt as the PCM further enhanced system performance due to Hitec's superior thermophysical properties. Key findings include:

- The optical efficiency of the RAC system is calculated as 58.8 %, and the receiver efficiency is 64.3 %. Additionally, the overall solar thermal conversion efficiency of the RAC receiver system is 22.8 %.
- In Model-I, 0.7 kg of Solar Salt and 3.8 kg of Hitec Salt were melted over 10 h. In contrast, Model-II achieved the melting of 3.1 kg of Solar Salt and complete melting of 18 kg of Hitec Salt, with salt temperatures reaching up to 455 K.
- The average mass flow rate of Hitec Salt in Model-II is measured at 0.72 g s^{-1}, and its average thermal efficiency of furnace is determined to be 23.8 % analytically, 26 % numerically, and 23 % experimentally. Also max thermal efficiency of furnace is reaching up to % 39.
- Average exergy efficiencies of the solar furnace were 11.5 % experimentally and 12.4 % numerically. Also max exergy efficiency of furnace is reaching up to % 20. The total exergy efficiency of the all system is calculated as approximately 7.5 %.
- The uncertainty in thermal efficiency is estimated at ± 3.4 %, and ± 1.3 % for exergy efficiency.

The experimental validation confirmed strong agreement with analytical and numerical results, supporting the accuracy of the proposed design. Additionally, it was demonstrated that the system could store thermal energy for over 11 h including 7 h of charging and 4 h of discharging.

The thermal energy stored in the RAC-furnace system has potential for diverse applications, particularly in regions with high solar irradiance. It may support residential or industrial heat demands and can be integrated into hybrid systems. Future developments may include coupling the furnace with a heat exchanger to transfer the stored energy to external loads efficiently.

Compared to conventional parabolic dish systems, the RAC design offers several practical advantages most notably, a lower and more accessible focal point that facilitates solar tracking, heat storage, and thermal process applications. While traditional CSP systems are designed for large-scale power generation, the proposed RAC-furnace system is a viable alternative for both individual and large-scale thermal energy applications.

CRediT authorship contribution statement

Ali Kemal Özcan: Writing – review & editing, Writing – original draft, Visualization, Validation, Software, Resources, Methodology, Investigation, Formal analysis, Data curation. **Cevdet Demirtaş:** Supervision, Project administration, Formal analysis, Conceptualization. **Betül Saraç:** Writing – review & editing, Visualization, Supervision.

Declaration of competing interest

The authors declare that they have no known competing financial interests or personal relationships that could have appeared to influence the work reported in this paper.

Acknowledgements

This article was financial supported give in by Council of Higher Education YOK 100/2000 Project and The Scientific and Technological Research Council of Türkiye (TUBITAK BIDEB).

Data availability

No data was used for the research described in the article.

References

[1] Mwesigye A, Huan Z, Meyer JP. Thermal performance and entropy generation analysis of a high concentration ratio parabolic trough solar collector with Cu-Therminol VP-1 nanofluid. Energ Conver Manage 2016;120:449–65. https://doi.org/10.1016/j.enconman.2016.04.106.
[2] Achahour O, Ghazzani BE, Safoi R, Eddemani A, Abbassi M, Elfanaoui A, et al. Experimental investigation on linear Fresnel reflector prototype for solar heat production. J Renew Energy Sustain Dev (RESD) 2025;11(1). https://doi.org/10.21622/RESD.2025.11.1.1277.
[3] Umar AB, Gupta MK, Buddhi D. Concentrated solar thermal power technologies: a review. J Crit Rev 2021;7(19):8162–84. https://doi.org/10.31838/jcr.07.19.922.
[4] Vasylyev, S., Vasylyev, V., & Sergeev, V. Concept and Design of Flat- Plate CPV Module Based on Ring-Array. 35th IEEE Photovoltaic Specialists Conference (2010) USA: IEEE. doi:10.1109/PVSC.2010.5614474.
[5] Garcia D, Liang D, Tibúrcio BD, Almeida J, Vistas CR. A three-dimensional ring-array concentrator solar furnace. Sol Energy 2019;193:915–28. https://doi.org/10.1016/j.solener.2019.10.016.
[6] Garcia D, Liang D, Almeida J, Tibúrcio B, Costa H, Catela M, et al. Analytical and numerical analysis of a ring-array concentrator. Int J Energy Res 2021. https://doi.org/10.1002/er.6787.
[7] Ky TSM, Sorgho I, Sawadogo S, Dabilgou D, Ouédraogo S, Ouédraogo A, et al. Conception, realization and testing of a solar cooker built with ring array concentrator - RAC in sub Saharan region. Sol Compass 2023;7:100056. https://doi.org/10.1016/j.solener.2024.112497.
[8] Cabeza L, Castell A, Barreneche C, Gracia A, Fernández A. Materials used as PCM in thermal energy storage in buildings: a review. Renew Sustain Energy Rev 2011;15:1675–95. https://doi.org/10.1016/j.rser.2010.11.018.
[9] Jiang Z, Jiang F, Li C, Leng G, Zhao X, Li Y, et al. A form stable composite phase change material for thermal energy storage applications over 700 C. Appl Sci 2019. https://doi.org/10.3390/app9050814.

[10] Tao P, Chang C, Tong Z, Bao H, Song C, Wu J, et al. Magnetically-accelerated large-capacity solar-thermal energy storage within high-temperature phase-change materials. Energy Environ Sci 2019:1613–21. https://doi.org/10.1039/C9EE00542K.
[11] Bellos E, Bousi E, Tzivanidis C, Pavlovic S. Optical and thermal analysis of different cavity receiver designs for solar dish concentrators. Energy Convers Manage: X 2019:100013. https://doi.org/10.1016/j.ecmx.2019.100013.
[12] Kasaeian A, Kouravand A, Rad M, Maniee S, Pourfayaz F. Cavity receivers in solar dish collectors: a geometric overview. Renewable Energy (169) 2021:53–79. https://doi.org/10.1016/j.renene.2020.12.106.
[13] Verma S, Das R. Performance analysis of a solar still driven by a packed bed thermal storage tank during off sunshine period. J Storage Mater 2021;44:103381. https://doi.org/10.1016/j.est.2021.103381.
[14] Verma S, Banerjee S, Das R. A fully analytical model of a box solar cooker with sensible thermal storage. Sol Energy 2022;233:531–42. https://doi.org/10.1016/j.solener.2021.12.035.
[15] Asgari M, Javidan M, Nozari M, Asgari A, Ganji D. Simulation of solidification process of phase change materials in a heat exchanger using branch-shaped fins. Case Stud Therm Eng 2021;25:100835. https://doi.org/10.1016/j.csite.2020.100835.
[16] Ma L, Zhang C, Wu Y, Lu Y. Comparative review of different influence factors on molten salt corrosion characteristics for thermal energy storage. Sol Energy Mater Sol Cells 2022;235:111485. https://doi.org/10.1016/j.solmat.2021.111485.
[17] Kruizenga, A.M., Gill, D.D., LaFord, M. & McConohy, G., Corrosion of High Temperature Alloys in Solar Salt at 400, 500, and 680°C, SANDIA National Laboratories, Technical Report, Doi: 10.2172/1104752.
[18] Zhu M, Zeng S, Zhang H, Li J, Cao B. Electrochemical study on the corrosion behaviors of 316 SS in HITEC molten salt at different temperatures. Solar Energy Mater Solar Cells 2018;186:200–7. https://doi.org/10.1016/j.solmat.2018.06.044.
[19] Li N, Wang W, Liu Q, Peng H. Evaluation of thermal-physical properties of novel multicomponent molten nitrate salts for heat transfer and storage. Energies 2022;15:6591. https://doi.org/10.3390/en15186591.
[20] Bauer, T., Laing, D., & Tamme, R. Overview of PCMs for concentrated solar power in the temperature range 200 to 350 °C. Advances in Science and Technology, Volume 74, (2010) 5th Forum on New Materials, part of CIMTEC (s. 272-277). Switzerland: Trans Tech Publications Ltd. Doi: 10.4028/www.scientific.net/AST.74.272.
[21] Ivenson B, Broome S, Kruizenga A, Cordaro J. Thermal and mechanical properties of nitrate state thermal storage salts in the solid-phase. Sol Energy 2012;86:2897–911. https://doi.org/10.1016/j.solener.2012.03.011.
[22] Karathanasis, S. (2019). Linear Fresnel Reflector Systems for Solar Radiation Concentration (ISBN 978-3-030-05279-9), Springer. Doi: 10.1007/978-3-030-05279-9.
[23] Stine, W., & Diver, R. (1994). A Compendium of Solar Dish/Stirling Technology. California, US: Sandia National Laboratories. Doi: 10.2172/10130410.
[24] Steinfeld A. Concentrated solar energy – the path for efficient thermal conversion to power and fuels. Sci. Bullet. 2019;64(8):485–6. https://doi.org/10.1016/j.scib.2019.04.012.
[25] Jaramillo SOA. Transporte de energia solar concentrada a travesde fibras opticas: acoplamiento fibra-concentrador y estudio termico. Morelos, Mexico: Universidad Nacional Autónoma de México; 1998. https://hdl.handle.net/20.500.14330/TES01000263220.
[26] Tetreault-Friend M, Gray L, Berdibek S, McKrell T, Slocum A. Optical properties of high temperature molten salt mixtures for volumetrically absorbing solar thermal receiver applications. Sol Energy 2017;153:238–48. https://doi.org/10.1016/j.solener.2017.05.054.
[27] Xie M, Zhu Y, Liu Y, Yuan Y, Tan H. Measurement of spectral radiative characteristics of molten salt at high temperature using emission method. Appl Therm Eng 2019;149:151–64. https://doi.org/10.1016/j.applthermaleng.2018.12.046.
[28] Touloukian, Y. S., ve DeWitt, D. P. (1970). Thermophysical properties of matter - the TPRC data series.Thermal radiative properties - metallic elements and alloys. United stated.
[29] Goswami, D. Y. (2015). Princibles of Solar Engineering (CRC Press b.). Boca Raton, London, New York: Taylor & Francis Group, Doi: 10.1201/b18119.
[30] Whillier A. The determination of hourly values of total solar radiation from daily summations. Arch Met Geophys Biokl 1956;B7:197–204. https://doi.org/10.1007/BF02243322.
[31] Liu BY, Jordan RC. The interrelationship and characteristic distribution of direct, diffuse and total solar radiation. Solar Energy 1960;4(3):1–19. https://doi.org/10.1016/0038-092X(60)90062-1.
[32] Iqbal, M. (1983). An Introduction to Solar Radiation (Academic press b.). Vancouver, Canada. Doi: 10.1016/B978-0-12-373750-2.X5001-0.
[33] Gueymard C. Prediction and performance assessment of mean hourly global radiation. Sol Energy 2000;68(3):285–303. https://doi.org/10.1016/S0038-092X(99)00070-5.
[34] Collares-Pereira M, Rabl A. The average distribution of solar radiation-correlations between diffuse and hemispherical and between daily and hourly insolation values. Solar Energy 1979;22(2):155–64. https://doi.org/10.1016/0038-092X(79)90100-2.
[35] Kaygusuz K. Calculation of solar radiation data on horizontal and tilted surfaces for Trabzon, Turkey. J Eng Res Appl Sci 2020;9(2):1471–6. http://www.journaleras.com/index.php/jeras/article/view/215.
[36] Lohrasbi S, Sheikholeslami M, Ganji DD. Discharging process expedition of NEPCM in fin-assisted Latent Heat thermal Energy Storage System. J Mol Liq 2016;221:833–41. https://doi.org/10.1016/j.molliq.2016.06.044.
[37] Duffie, J. A., & Beckman , W. A. (2013). Solar engineering of thermal processes. John Wiley & Sons, Doi: 10.1002/9781118671603.
[38] Castellanos LM, Caballero GC, Cobas VM, Lora ES, Reyes AM. Mathematical modeling of the geometrical sizing and thermal performance of a Dish/Stirling system for power generation. Renew Energy 2017;107:23–35. https://doi.org/10.1016/j.renene.2017.01.020.
[39] Sansaniwal SK, Sharma V, Mathur J. Energy and exergy analyses of various typical solar energy applications: a comprehensive review. Renew Sustain Energy Rev 2018;82:1576–601. https://doi.org/10.1016/j.rser.2017.07.003.
[40] Lane, G. A. Solar Heat Storage Latent Heat Materials, Vol 1 Background and Scientific Principles. J. Solar Energy Eng. (1983), Midland, USA: CRC Press, Doi: 10.1115/1.3266412.
[41] Sharma A, Tyagi VV, Chen CR, Buddhi D. Review on thermal energy storage with phase change materials and applications. India. Renew Sustain Energy Rev 2009;13. https://doi.org/10.1016/j.rser.2007.10.005.
[42] Dinçer İ., Rosen, M. (2011). Thermal energy storage: Systems and applications (2. Edition), Hoboken, N.J.: Wiley. 10.1002/9780470970751.
[43] Subramaniam SB, Senthil R. Heat transfer enhancement of concentrated solar absorber using hollow cylindrical fins filled with phase change material. Int J Hydrogen Energy 2021;4:6. https://doi.org/10.1016/j.ijhydene.2021.04.061.
[44] MacPhee D, Dinçer I. Thermal modeling of a packed bed thermal energy storage system during charging. Appl Therm Eng 2009;29:695–705. https://doi.org/10.1016/j.applthermaleng.2008.03.041.
[45] Cengel YA, Boles MA. Thermodynamics: An Engineering Approach. 5. New York: McGraw Hill; 2006.
[46] Petela R. Exergy of undiluted thermal radiation. Sol Energy 2003;74(6):469–88. https://doi.org/10.1016/S0038-092X(03)00226-3.
[47] Hassab M, Sorour M, Mansour M, Zaytoun M. Effect of volume expansion on the melting process's thermal behavior. Appl Therm Eng 2017;115:350–62. https://doi.org/10.1016/j.applthermaleng.2016.12.006.
[48] Arıcı M, Tütüncü E, Kan M, Karabay H. Melting of nanoparticle-enhanced paraffin wax in a rectangular enclosure with partially active walls. Int J Heat Mass Transf 2017;104:7–17. https://doi.org/10.1016/j.ijheatmasstransfer.2016.08.017.
[49] Chauhan V, Yadav A, Soni S. Simulation of Melting Process of a phase Change Material (PCM) using ANSYS (Fluent). Int Res J Eng Technol (IRJET) 2017;04(05). p. 3289–3294.www.irjet.net.
[50] Voller V, Prakash C. A fixed-grid numerical modeling methodology for convection-diffusion mushy region phase-change problems. Int J Heat Mass Transf 1987;30:1709–20. https://doi.org/10.1016/0017-9310(87)90317-6.
[51] Zhang P, Xiao X, Meng Z, Li M. Heat transfer characteristics of a molten-salt thermal energy storage unit with and without heat transfer enhancement. Appl Energy 2015;137:758–72. https://doi.org/10.1016/j.apenergy.2014.10.004.
[52] Kline S, McClinton F. Describing Uncertainties in Single-Sample Experiment. Mech Eng 1953;75:3–8.
[53] Mahfuz M, Kamyar A, Afshar O, Sarraf M, Anisur M, Kibria M, et al. Exergetic analysis of a solar thermal power system with PCM storage. Energy Convers Manage 2014;78:486–92. https://doi.org/10.1016/j.enconman.2013.11.016.
[54] Turrini S, Bettonte M, Eccher M, Grigiante M, Miotello A, Brusa RS. An innovative small-scale prototype plant integrating a solar dish concentrator with a molten salt storage system. Renew Energy 2018;123:150–61. https://doi.org/10.1016/j.renene.2018.02.053.
[55] Khan MI, Gutierrez-Alvarez R, Asfand F, Bicer Y, Sgouridis S, Al-Ghamdi SG, et al. The economics of concentrating solar power (CSP): Assessing cost competitiveness and deployment potential. Renew Sustain Energy Rev 2024;200:114551. https://doi.org/10.1016/j.rser.2024.114551.
[56] Rosen M, Dincer I. Exergoeconomic analysis of power plants operating on various fuels. Appl Therm Eng 2003;23:643–58. https://doi.org/10.1016/S1359-4311(02)00244-2.